

# Tuning Threshold Voltage in Organic Electrochemical Transistors by Varying Doping of the Conjugated Polymer p(g3T2-T)

Marielena Velasco Enriquez

Thesis submitted for the degree of  
Erasmus Mundus Master of Science  
in Nanoscience and Nanotechnology,  
graduation option Nanoelectronics

**Supervisors:**  
Prof. Dr. Karl Leo  
Prof. Dr. Steven De Feyter

**Assessor:**  
PD Dr.rer.nat.habil. Hans Kleemann

**Assistant-supervisor:**  
MSc. Anton Weissbach

© Copyright KU Leuven

Without written permission of the supervisors and the author it is forbidden to reproduce or adapt in any form or by any means any part of this publication. Requests for obtaining the right to reproduce or utilize parts of this publication should be addressed to Faculteit Ingenieurswetenschappen, Kasteelpark Arenberg 1 bus 2200, B-3001 Leuven, +32-16-321350.

A written permission of the supervisors is also required to use the methods, products, schematics and programmes described in this work for industrial or commercial use, and for submitting this publication in scientific contests.

# Preface

*Marielena Velasco Enríquez*

# Contents

<b>Preface</b>	<b>i</b>
<b>Abstract</b>	<b>iv</b>
<b>List of Figures</b>	<b>v</b>
<b>List of Tables</b>	<b>vi</b>
<b>1 Introduction</b>	<b>1</b>
<b>2 Background</b>	<b>3</b>
2.1 Organic Semiconductors . . . . .	3
2.1.1 Electronic Structure and Transport . . . . .	3
2.1.2 Molecular Doping . . . . .	4
2.2 Organic Mixed Ionic/Electronic Conductors (OMIECs) . . . . .	6
2.2.1 Processes in OMIECs . . . . .	8
2.3 Organic Electrochemical Transistors . . . . .	10
2.3.1 Device Physics . . . . .	10
2.3.2 Operation Modes . . . . .	11
2.3.3 Important Figures of Merit . . . . .	14
2.3.4 Side Reactions . . . . .	17
<b>3 Experimental Methods</b>	<b>19</b>
3.1 Materials . . . . .	19
3.2 Equipment . . . . .	20
3.3 Software . . . . .	21
3.4 Photomask . . . . .	22
3.5 Experimental Procedure . . . . .	22
3.5.1 Preparation of Films . . . . .	22
3.5.2 Doping Characterization of Films . . . . .	23
3.5.3 Fabrication of Organic Electrochemical Transistors . . . . .	24
<b>4 Results and Discussion</b>	<b>31</b>
4.1 Doping Characterization . . . . .	31
4.1.1 Thickness, Sheet Resistance and Resistivity . . . . .	31
4.1.2 Absorbance and Dopants Diffusion . . . . .	32
4.1.3 Workfunction . . . . .	33
4.2 Fabrication of Organic Electrochemical Transistors . . . . .	34
4.2.1 Influence of Doping on OECT Channel . . . . .	35

---

## CONTENTS

4.2.2	Stability on Air of p(g3T2-T) . . . . .	38
4.2.3	Reverse Oxidation of Undoped-p(g3T2-T) . . . . .	40
4.2.4	Solid-OECTs using Undoped-p(g3T2-T) . . . . .	41
4.2.5	Solid-OECTs using Doped-p(g3T2-T) . . . . .	47
4.2.6	Shift of OECT Threshold Voltage . . . . .	48
<b>5</b>	<b>Conclusions and Outlook</b>	<b>49</b>
<b>A</b>	<b>Absorption of p(g3T2-T) Doped with F6TCNNQ</b>	<b>51</b>
<b>B</b>	<b>PEDOT:PSS vs Doped p(g3T2-T) as Channel</b>	<b>53</b>
	<b>Bibliography</b>	<b>55</b>

# Abstract

Organic Electrochemical Transistors (OECTs) exhibit advantageous properties, such as high transconductance and steep-slope switching, while operating at very low voltages. Although, their switching speed is comparatively slower than solid-state devices, it remains sufficient for applications in bioelectronics [1]. The gold standard conjugated polymer for p-type OECTs is PEDOT:PSS. However, its main drawback lies in its depletion-mode operation, which requires power to turn off the device. To minimize power consumption and improve stability, efforts have been made to the design conjugated polymers that allow accumulation-mode devices. One such polymer, 3-(2-(2-methoxyethoxy)ethoxy)thiophene (p(g3T2-T)) has demonstrated negative threshold voltages close to zero and high transconductance [2]. Furthermore, by doping p(g3T2-T) at various levels and drop-casting it as a gate, it has been possible to fine-tune the threshold voltage [3]. This study aims to adapt a microstructuring method for fabricating side-gated OECT devices that comprise different doping levels of F<sub>4</sub>TCNQ and F<sub>6</sub>TCNNQ in p(g3T2-T) and a solid-state electrolyte [4], the latter is deposited by inkjet printing. Additionally, the study aims to adjust the threshold voltage by utilizing these varying doping levels, while analyzing the stability and performance of the doped devices.

# List of Figures

2.1	Energy level diagram of organic semiconductors . . . . .	3
2.2	Degenerate and non-degenerate conjugated polymers . . . . .	4
2.3	Scheme of doping processes in organic semiconductors . . . . .	5
2.4	Representation of bipolaron formation introduced via doping . . . . .	5
2.5	Formation of polaron, bipolaron, and bipolaron band . . . . .	6
2.6	Material classes of OMIECs . . . . .	7
2.7	Electronic transport mechanisms in OMIECs . . . . .	8
2.8	Ionic transport mechanisms in OMIECs . . . . .	9
2.9	Device physics of MOSFET vs OECT . . . . .	10
2.10	Typical OECT structure and circuit model . . . . .	11
2.11	Depletion- and accumulation-mode OECTs . . . . .	12
2.12	Chemical structure of polymer g2T-T . . . . .	13
2.13	Chemical structure and transconductance of g2T-T with side-chain engineering . . . . .	13
2.14	OECTs benchmark with different OMIECs . . . . .	15
2.15	Tuning of threshold voltage with different levels of doping p(g3T2-T) . . . . .	16
2.16	Energy levels of neutral state of OMIECs related to oxygen reduction reactions potentials . . . . .	18
3.1	Used photomask for fabricated OECT gold electrodes. . . . .	22
3.2	Chemical structures of the repeat units of p(g3T2-T) and F <sub>4</sub> TCNQ dopant. . . . .	23
3.3	Dynamic spin-coating process to obtain undoped and doped films of p(g3T2-T)). . . . .	23
3.4	Visualization of the workflow for Au-contacts patterning. . . . .	25
3.5	Visualization of the workflow for patterning undoped p(g3T2-T). . . . .	25
3.6	Visualization of the workflow for patterning doped p(g3T2-T). . . . .	26
3.7	Representation of experimental setup for measuring threshold voltage shift of a single OECT under ambient conditions. Scheme is not drawn to scale. . . . .	26
3.8	Chemical structures of the repeat units of p(g3T2-T) and F <sub>6</sub> TCNNQ dopant. . . . .	27
3.9	Solid-OECT fabrication with undoped p(g3T2-T) . . . . .	29
3.10	Solid-OECT fabrication with doped p(g3T2-T) . . . . .	29
4.1	Color shift upon doping level increase . . . . .	31

## LIST OF FIGURES

---

4.2	Sheet resistance and resistivity drop upon doping . . . . .	32
4.3	Absorbance spectra of different doping levels of p(g3T2-T) . . . . .	33
4.4	Representation of the Fermi level shift upon doping . . . . .	34
4.5	Micrographs of a patterned channel and gate p(g3T2-T) at different doping levels . . . . .	34
4.6	Transfer characteristics and transconductance at different doping levels and $V_{DS}$ . . . . .	36
4.7	Transfer characteristics comparing different doping levels . . . . .	37
4.8	Threshold shift at different doping levels and $V_{DS}$ . . . . .	38
4.9	Drain current over time of undoped-p(g3T2-T) coupled with SSE precursor	39
4.10	Transfer characteristics after electrochemical de-doping . . . . .	40
4.11	Electrochemical de-doping of oxidized p(g3T2-T) OECT . . . . .	41
4.12	Performance of solid-OECT with drop-casted SSE . . . . .	43
4.13	Performance of solid-OECT with photolithographed SSE . . . . .	45
4.14	Performance of solid-OECT with printed SSE . . . . .	46
4.15	Performance of solid-OECT with doped-p(g3T2-T) . . . . .	48

# List of Tables

2.1	Volumetric capacitance (C*) of various OECTs channel materials . . . . .	14
3.1	Cyclic Voltammetry parameters. . . . .	21
3.2	Electrochemical Impedance Spectroscopy parameters. . . . .	22
3.3	Composition of the solid-state electrolyte [4]. . . . .	26
3.4	Composition of adhesion promoter. . . . .	28
4.1	Sheet resistance and resistivity values for undoped and doped films of p(g3T2-T) . . . . .	31
4.2	Calculated workfunction from UPS measurements and represented in Figure 4.4. . . . .	33
4.3	Maximum transconductance values extracted from Figure 4.6 . . . . .	37
4.4	Threshold voltage extracted from Figure 4.10 . . . . .	40
4.5	Parameters extracted from the characterization of drop-casted SSE OECT	43
4.6	Parameters extracted from the characterization of photopatterned SSE OECT under $N_2$ environment. . . . .	44
4.7	Parameters extracted from the characterization of photopatterned SSE OECT under ambient conditions . . . . .	45
4.8	Parameters extracted from the characterization of printed SSE OECT .	46
4.9	Parameters extracted from the characterization of doped-p(g3T2-T) OECT	47



# Chapter 1

## Introduction

The field of organic electronics has witnessed significant advancements in recent years due to its potential biocompatibility, mechanical compliant, and other application-specific characteristics. Among the numerous types of organic devices, Organic Electrochemical Transistors (OECTs) have attracted considerable attention due to their unique capabilities such as high transconductance and steep-slope switching at low operation voltages, which give them potential for use in energy storage, bioelectronics, and neuromorphic devices.

Accumulation-mode transistors, devices that are normally in the OFF state at zero-gate-biased condition, rely on the use of undoped conjugated polymers. In contrast, the ability to precisely control and tune the threshold voltage of an OECT can be achieved by manipulating the doping level of the mentioned conjugated polymer as shown by Tan et al. [3]. However, they fabricated devices that did not follow a complete microstructuring technique, limiting their integration into circuits.

The primary objective of this research is to address this missing information by developing a microstructuring method to fabricate accumulation-mode OECTs with controlled doping levels and enable their seamless integration into circuits. However, during the pursuit of this objective, it was identified that stability of the polymer and dopants in an electrochemical environment may pose challenges that need to be addressed as well. Therefore, this research project specifically aims to:

1. Characterize 3-(2-(2-(2-methoxyethoxy)ethoxy)ethoxy)thiophene (p(g3T2-T)) with varying doping levels of F<sub>4</sub>TCNQ and F<sub>6</sub>TCNNQ. This involves modifying the conjugated polymer film with different concentrations of dopant and analyzing their electronic structure, morphology and electrical properties using techniques such as UV-Vis spectroscopy, Ultraviolet Photoelectron Spectroscopy (UPS), Van Der Pauw method, Electrical Impedance Spectroscopy (EIS) and Cyclic Voltammetry (CV),
2. fabricate OECT devices, which involves utilizing the conjugated polymer at different doping levels, and adapting an existing method that combines electrode patterning techniques, spin-coating, photolithography and inkjet printing. The devices will be carefully optimized to ensure reproducibility and stability,

## 1. INTRODUCTION

---

3. assess doped polymer stability in OECTs, which involves performing conductivity measurements over time and selecting an electrolyte composition that allows a stable performance, and
4. investigate the shift in threshold voltage through electrical characterization of the fabricated OECT devices with varying doping levels of F<sub>4</sub>TCNQ and F<sub>6</sub>T<sub>2</sub>CNNQ.

The thesis is structured as follows: Chapter 1 provides an overview of organic electronics and the importance of the OECT threshold voltage, and outlines the motivation, goals, and structure of the thesis. Chapter 2 presents a comprehensive review of the relevant background information on Organic Semiconductors (OSCs), Organic Mixed Ionic Electronic Conductors (OMIECs), and Organic Electrochemical Transistors, and relevant research on tuning the threshold voltage of OECTs. Chapter 3 illustrates the Experimental Methods used in this research, describes the materials, equipment, software, and procedures to chemically dope the films and characterization method employed in the study. Finally, it outlines the fabrication and characterization process of OECT devices. In Chapter 4, the experimental results obtained are presented, from the characterization of the conjugated polymer at different doping levels and fabricated OECT devices. Analysis of the relationship between the doping level and the shift in threshold voltage. Finally, it discusses the implications of the findings and their relevance to the field. Lastly, Chapter 5 provides a summary of the research objectives and the extent to which they were achieved, suggests future research direction, and potential applications.

# Chapter 2

## Background

### 2.1 Organic Semiconductors

Unlike inorganic semiconductors, organic semiconductors are lightweight, easy to chemically tune, mechanically flexible, and offer low-cost and low-temperature processing. All of these characteristics are responsible for the increased attention to this type of material in the field of organic electronics.

#### 2.1.1 Electronic Structure and Transport

Organic semiconductors are  $\pi$ -conjugated molecules that comprise mostly carbon and hydrogen atoms, with alternating multiple ( $sp^2$  hybridization) and single ( $sp$  hybridization) bonds. The wavefunction of the  $sp^2$  orbitals overlap so that electrons are delocalized. Based on the size of the conjugated system, organic semiconductors can be divided into conjugated polymers and small molecules. The latter have the advantage that their synthesis and low molecular mass allows to obtain them high purity material [5].

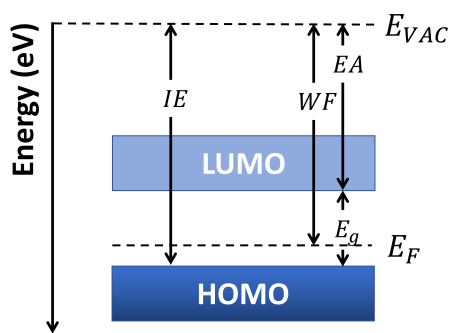


**Figure 2.1:** Energy level diagram of an p-type doped organic semiconductor.

The energy structure of organic semiconductors comprises a highest occupied molecular orbital (HOMO) state and a lowest unoccupied molecular orbital (LUMO) state, which are analogous to the valence and conduction bands, respectively, from

## 2. BACKGROUND

inorganic semiconductors. The difference between these energy levels corresponds to the energy gap ( $E_g$ ) of the material, as illustrated in Figure 2.1. Additionally, we can define i) the Fermi level ( $E_F$ ) using the material's work function (WF), ii) the ionization energy (IE), also referred as ionization potential (IP), using the HOMO energy, and iii) the electron affinity (EA), using the LUMO energy.

Organic semiconductor materials can also be classified based on whether their ground state is degenerate or non-degenerate. In the former case, the term "degenerate" describes monomers that have equivalent energy states in the ground state. In contrast, in the latter case, the ground state exhibits non-degeneracy, which is commonly observed due to the energy difference of aromatic (benzoid) and quinoid structures [6], as exhibited in Figure 2.2.

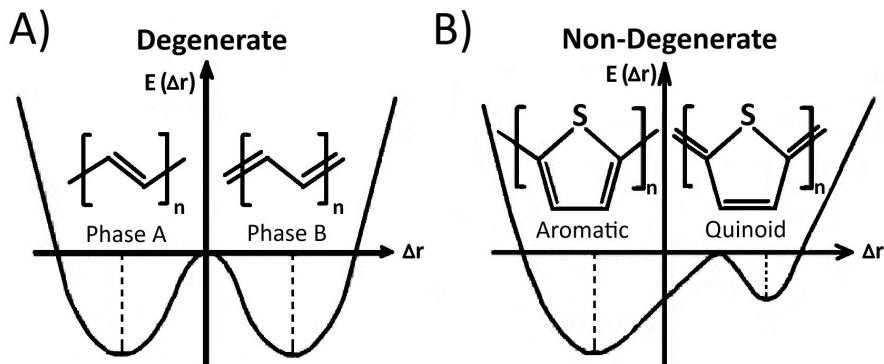


**Figure 2.2:** Potential energy change (electronic plus lattice distortion energy) in A) degenerate and B) non-degenerate ground-state-conjugated polymers. Extracted from reference [7].

In electronic transport theory for organic semiconductors, the concept of polarons is introduced. This quasiparticle effectively captures the alteration of the bond-length alternation pattern induced by the movement of charge carriers (electrons or holes) [8]. This alteration can be observed, for instance, when transitioning from Phase A to Phase B in degenerate molecules, or from aromatic to a quinoid structure in non-degenerate molecules.

### 2.1.2 Molecular Doping

The basic principles of molecular doping are similar than in inorganic materials. A donor or acceptor entity is added to generate electrons or holes, as shown in Figure 2.3. While n-type dopants donate electrons to the LUMO state, the p-type dopants extract electrons from the HOMO state, thus creating holes [9]. In other words, the Fermi level  $E_F$  of the polymer will shift towards the LUMO (or HOMO) level when there is n-type (or p-type) doping. This shift can be quantified using spectroscopy techniques such as Ultraviolet Photoelectron Spectroscopy (UPS) [10], although it may be somewhat limited by the penetration depth of the exciting electrons.

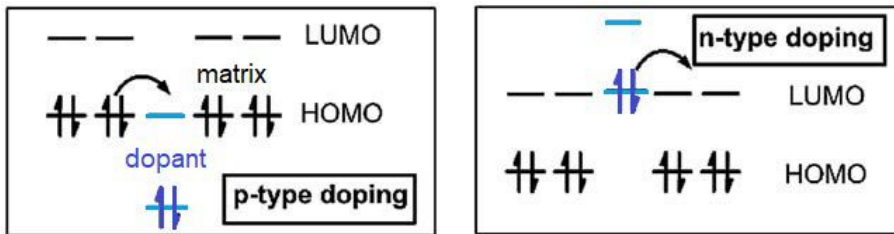


**Figure 2.3:** Schemes for p-type (left) and n-type (right) doping processes.

When doping occurs, the formation of a new quasiparticle named bipolaron occurs. For instance, if p-type dopants are introduced to a degenerate molecule (as depicted in Figure 2.4), electrons are removed from double bonds. Focusing on a single event, this removal leaves one carbon positively charged, with an adjacent carbon atom possessing an unpaired electron. This unpaired electron moves along the polymer chain until it encounters another unpaired electron from a separate doping event. When they come together, they form a double bond, resulting in the creation of two charged polarons: a bipolaron [11].

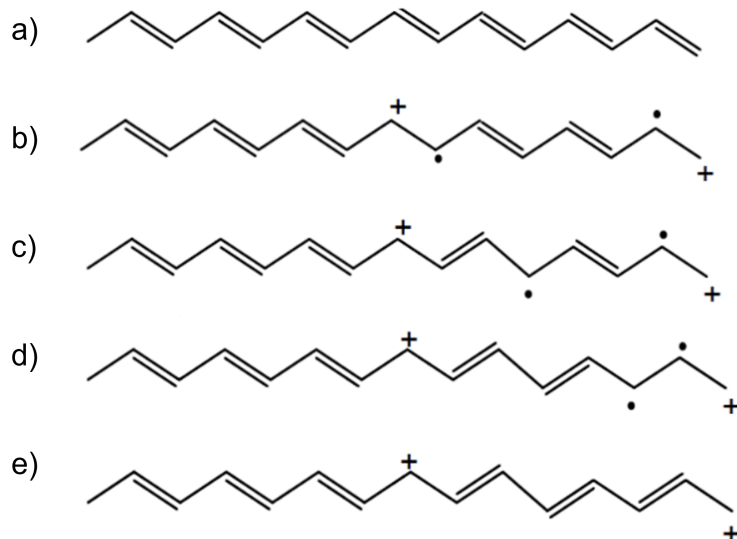


**Figure 2.4:** a) Structure of degenerate molecule. b) Electron extraction via doping. c) Unpaired electron shifting down. d) Unpaired electrons meet. e) Formation of double bond and two charged polarons: bipolaron.

The energy levels generated upon the formation of polarons and bipolarons in non-degenerate molecules are illustrated in Figure 2.5. As the doping density increases, the amount of bipolaron states also increases. Their overlapping leads to the formation of bipolaron bands, and the energy difference between the two in-gap states  $i$  and  $i^*$ , as shown from Figure 2.5B to D, decreases.

In addition to these new electronic states, the doped polymer will also exhibit

## 2. BACKGROUND

---

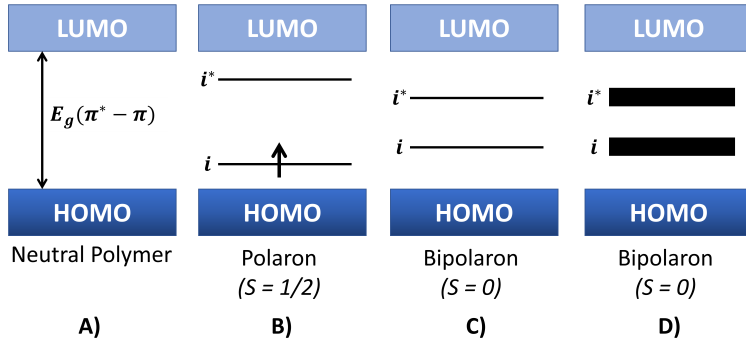


**Figure 2.5:** Potential energy change of aromatic and quinoid in the non-degenerate ground-state A) neutral conjugated polymer, and formation of B) polaron, C) bipolaron, and D) bipolaron bands upon doping. Extracted from reference [7].

distinct optical transitions that could be revealed through UV-Vis-NIR spectroscopy. In this technique, absorption peaks indicate the presence of these optical transitions. However, these transitions may not be precisely quantified or clearly defined [7].

The use of small molecules as dopants for organic materials is commonly reported. Some strong acceptor (or electron-deficient) molecules that are widely used include 2,3,5,6 tetrafluoro-7,7,8,8-tetracyanoquinodimethane ( $F_4TCNQ$ ) or 1,3,4,5,7,8 hexafluoro-7,7,8,8-tetracyanonaphthoquinodimethane ( $F_6TCNNQ$ ), both of which are also relevant to this work. The latter exhibits a higher electronic affinity (-5.3 eV) than  $F_4TCNQ$  (-5.2eV), indicating that it can abstract electrons more efficiently, specially from polymers with low ionization potential ( $IP < 5eV$ ) [12].

Among the various methods of molecular doping for conjugated polymers, Jacobs et al. conducted a comparison between solution-mixed and solution-sequential doping of P3HT, a thiophene-based polymer, doped with  $F_4TCNQ$ . These doping methods are considered straightforward and easy, especially when compared to other techniques such as vapor-phase doping [13]. Their research showed that solution-mixed films tend to have considerably rougher surface than solution-sequential films, which can negatively impact their conductivity [14]. The fact that solution-sequential doped films exhibit better homogeneity also makes them more compatible with microstructuring processes such as photolithography. Reason why it is going to be used in this work and will be further detailed in Section 3.5.1. However, this advantage comes at the expense of having less control over the doping levels when compared to solution-mixed films [15].

## 2.2 Organic Mixed Ionic/Electronic Conductors (OMIECs)

Organic Mixed Ionic/Electronic conductors are a class of organic semiconductors that allow the conduction of electrons (or holes) and ions. This feature sets them apart from other organic semiconductors. Commonly designed with polar side

## 2.2. Organic Mixed Ionic/Electronic Conductors (OMIECs)

chains, OMIECs have been identified as a promising class of materials for the field of bioelectronics [16]. Initially investigated for batteries and super-capacitors [17] [18], where the primary objective was to induce charges in a semiconducting polymer, OMIECs have rapidly expanded their scope to include other applications, among them, our focus: OECTs.

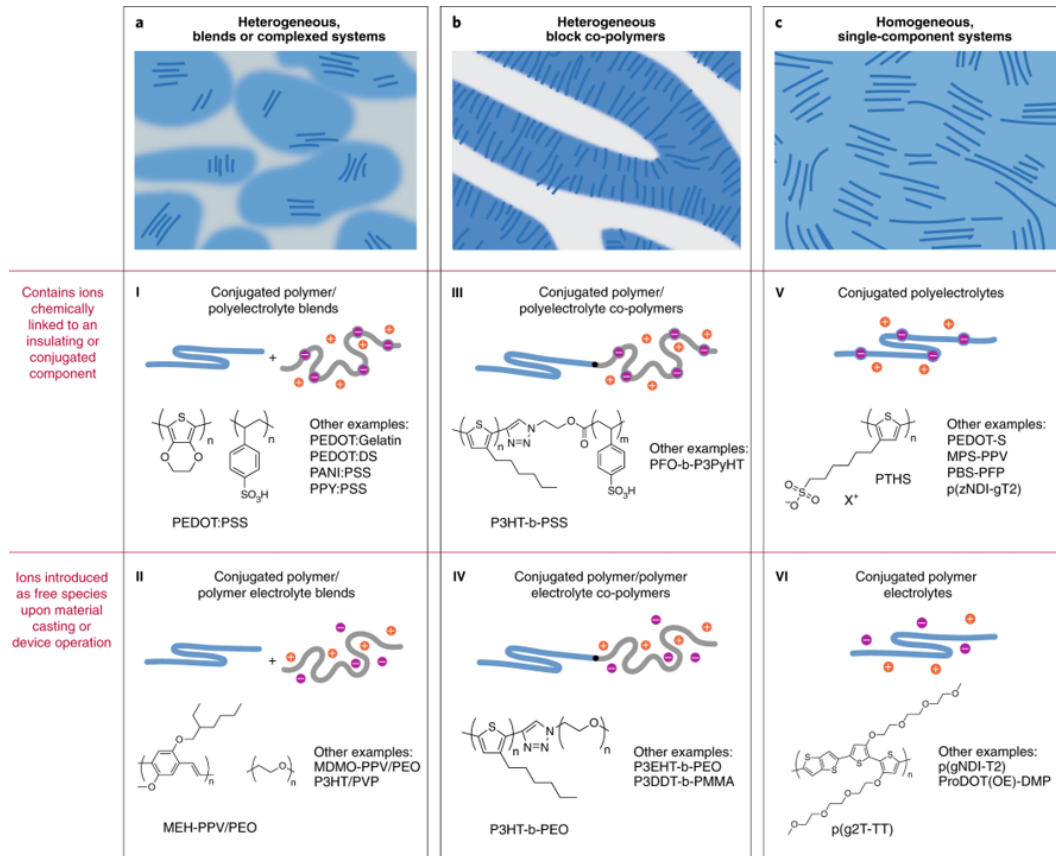


**Figure 2.6: OMIECs classes.** a) Heterogeneous blends of a conducting conjugated polymer with (I) a polyelectrolyte or (II) an ion-solvating polymer electrolyte. b) Heterogeneous block copolymers of a conducting conjugated polymer with (III) a polyelectrolyte or (IV) an ion-solvating polymer electrolyte. c) Fully conjugated (V) polyelectrolytes and (VI) ion-solvating polymer electrolytes. Extracted from reference [19].

Paulsen et al. classified OMIECs into six different categories based on whether they “*intrinsically contain ionic charge*” (I, III, V) or not (II, IV, VI), the latter group comprises materials that “*contain polar moieties that can solvate ions*”. Another distinguishing factor among these categories is whether the conjugated system is composed of a single material (homogeneous, type V and VI) or a two-component, more complex systems or block co-polymer materials (heterogeneous, type I, II, III, IV)[19]. A schematic representation is shown in Figure 2.6.

## 2. BACKGROUND

### 2.2.1 Processes in OMIECs

### 2.2.1.1 Ionic-electronic interactions

The presence of electronic charges in OMIECs requires also the presence of excess ionic charge, so charge in the system remains in balance. In the case of types II, IV, and VI OMIECs, a phenomenon known as stabilizing electrochemical doping is achieved through the presence of mobile ions that act as free charges. Conversely, other types of OMIECs have these stabilizing charges chemically bound and fixed, making them inherently doped.

The degree of coupling between electronic charges and excess ionic charges in OMIECs can be modulated by applying a bias when connected through an electrolyte [19]. This fundamental principle forms the basis of OECTs, which will be discussed further in Section 2.3.

### 2.2.1.2 Electronic transport

Electronic charge transport mechanisms present in OMIECs include thermally-activated hopping and band-like transport, as depicted in Figure 2.7. These mechanisms are not different from those observed in other conjugated polymers.

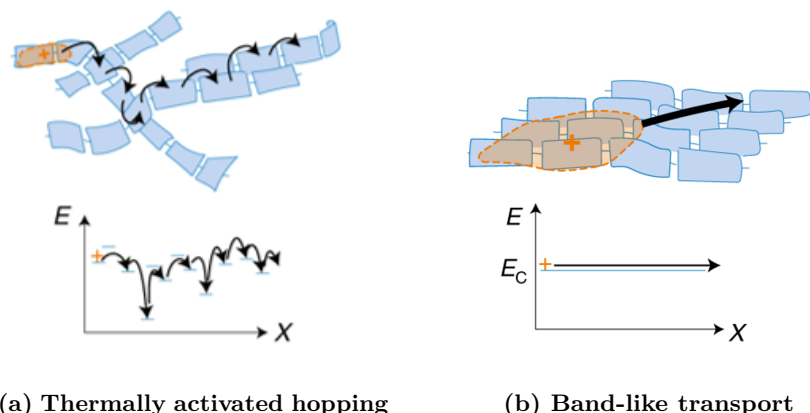


**Figure 2.7:** Schematic representation of electronic charge transport mechanisms: a) Thermally-activated hopping transport and b) band-like transport, where the electronic charge carrier is relatively localized and delocalized, respectively. Extracted from reference [19].

Thermally-activated hopping, as its name implies, is driven by thermal energy and is limited by the degree of structural disorder. In this mechanism, weakly-bonded electrons in delocalized  $\pi$ -orbital move along adjacent  $\pi$ -orbitals within the length of the conjugated polymer, or even between molecules where there is sufficient  $\pi$ - $\pi$  overlapping. This mechanism predominates when there is a low electronic charge carrier density and a low density of accessible hopping states, resulting in low mobility and electrical conductivity [19].

## 2.2. Organic Mixed Ionic/Electronic Conductors (OMIECs)

In contrast, band-like transport, typically occurs in OMIECs with increasing doping levels. In this case, the activation energy of charge hopping decreases, and carrier mobility increases. This leads to diffuse band-like charge transport within the polymer-stacking [20].

### 2.2.1.3 Ionic transport

While transport of anions and cations in OMIECs shares some similarities with the transport of electrons and holes, it is a more complex process, since ions can be “*multi-valent, and form pairs and larger clusters; moreover, they are sensitive to solvent and solvation*” [19].

Ion transport in dry OMIECs of type I, III, and V is unipolar because these ions are fixed on a polyelectrolyte. In contrast, in type II, IV, and VI OMIECs, both anions and cations are mobile. When OMIECs come into contact with an electrolyte, they tend to swell, allowing the penetration of excess ions from the electrolyte. Therefore, both mobile anions and cations contribute to ion transport to ensure electroneutrality.

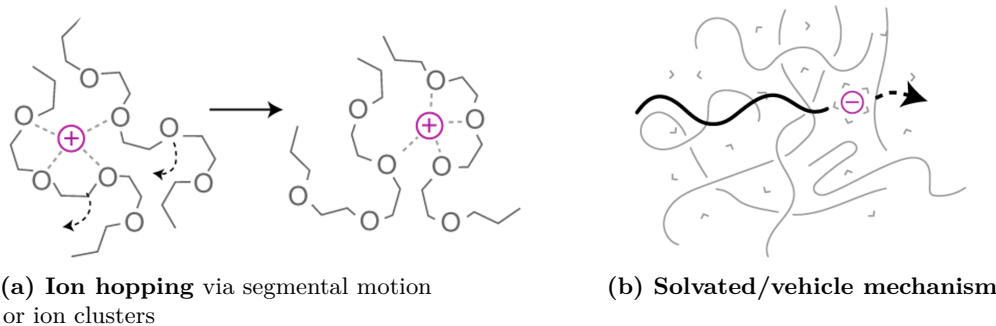


**Figure 2.8:** Schematic representation of ionic charge transport mechanisms: a) Ion hopping via segmented motion and b) vehicular solvated-ion transport. Extracted from reference [19].

There are two types of ionic charge transport in OMIECs: ion hopping and vehicular solvated-ion transport. In dry or minimally hydrated OMIECs, ion hopping assisted by segmental motion of the OMIEC side chains or backbone is the primary mechanism, as shown in Figure 2.8A. However, when OMIECs are in contact with a solvent or liquid electrolyte, both mechanisms are present, with solvated ion vehicle transport being the predominant mode. For instance, in water-based electrolytes, proton diffusion occurs via the Grotthuss mechanism, where protons within water molecules diffuse through neighboring molecules. This involves a transfer of ionic effects through the hydrogen-bonded network, as shown in Figure 2.8B.

Due to the existing ionic-electronic coupling, both ionic and electronic transport in OECTs and other OMIEC-electrolyte-based applications are not independent but are rather complex and must consider side effects such as hydration and electrolyte swelling [19], as will be further discuss in Section 2.3.

## 2. BACKGROUND

---

### 2.3 Organic Electrochemical Transistors

Organic Electrochemical Transistors are composed of metallic source, drain and gate electrodes, an organic conjugated polymer channel (specifically an OMIEC as described in previous sections), and an electrolyte that bridges the channel and the gate, as illustrated in Figure 2.10A. OECTs are devices that have received increasing attention due to their mechanical compliance, biocompatibility, and sensitivity to biochemical signals [21].

#### 2.3.1 Device Physics

Although the structural configuration of OECTs differs from conventional metal-oxide-semiconductor field-effect transistors (MOSFETs), understanding the operation of the latter can provide insight into how OECTs function. In contrast to MOSFETs, where an insulator is used, OECTs are coupled with an electrolyte, as shown in Figure 2.9. When a gate voltage is applied, instead of polarizing the dipoles in the insulator and creating a field that causes accumulation of carriers at the interface of the semiconductor/insulator, as is the case with MOSFETs, in OECTs, the gate voltage drives ions to penetrate the bulk of the channel. Consequently, accumulation of carriers occurs throughout the whole volume of the OMIEC film. This mechanism explains the large gate-channel capacitance observed in these devices compared to MOSFETs and why the drain current takes into account a volumetric capacitance [22].

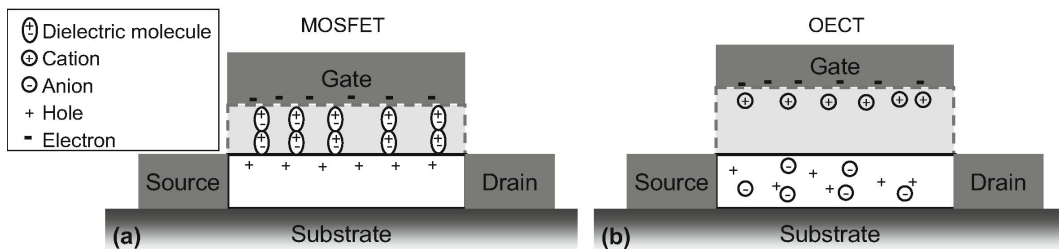


**Figure 2.9:** Comparison of p-type a) MOSFET and b) OECT, where the light-gray region represents an insulator and electrolyte, respectively. Extracted from reference [22]

Bernards and Malliaras implemented a model based on a p-type depletion-mode OECT (based on PEDOT:PSS as it is widely studies and fabricated material, further discussion in the following section) [23]. The model divides the behavior of the OECT into two circuits: an electronic circuit (comprising the source-channel-gate structure) and an ionic circuit (comprising the gate-electrolyte-channel structure).

The electronic circuit is treated as a *variable* resistor and is thus modeled using Ohm's law. Its variability arises from the fact that when a positive gate voltage is applied, de-doping of the semiconductor occurs, which is analogous to the compensation doping observed in silicon. Cations from the electrolyte penetrate the polymer, compensating for an acceptor.

Meanwhile, the ionic circuit consists of a resistor that represents the flow of ions in the electrolyte, connected in series with a capacitor representing the storage of ions in the channel, as shown in Figure 2.10B [1][23].

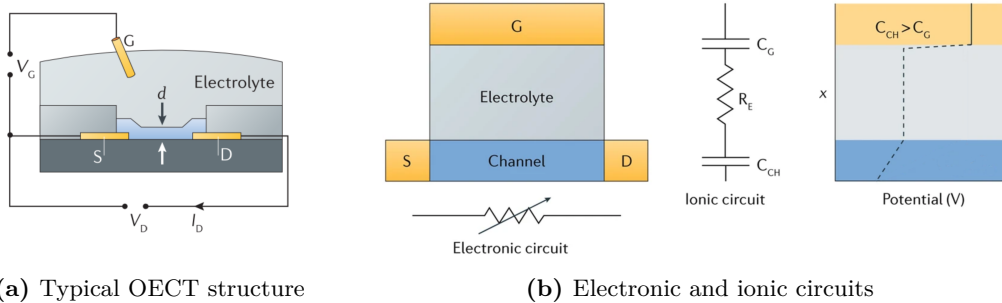


**Figure 2.10:** a) Typical structure of an organic electrochemical transistor. b) (Left) Electronic circuit modelled as a resistor with a variable resistance. (Right) Ionic circuit consisting of channel ( $C_{CH}$ ) and gate ( $C_G$ ) capacitors, coupled with a resistor corresponding to the electrolyte ( $R_E$ ). Extracted from reference [1].

Finally, the drain current  $I_D$  for the steady state behavior of the OEET can now be described using the following equation:

$$I_D = \begin{cases} -\mu C^* \left[ \frac{Wd}{L} \frac{V_{GS} - V_{Th}^2}{2V_{Th}} \right] & |V_{DS}| < |V_{GS}| - |V_{Th}| \\ -\mu C^* \frac{Wd}{L} \left[ 1 - \frac{V_{GS} - 1/2V_{DS}}{V_{Th}} \right] V_{DS} & |V_{DS}| > |V_{GS}| - |V_{Th}| \end{cases} \quad (2.1)$$

where  $\mu$  is the charge mobility,  $C^*$  is the volumetric capacitance and  $W$ ,  $d$  and  $L$  are the width, thickness and length of the channel.  $V_{GS}$ ,  $V_{DS}$  and  $V_{Th}$  correspond to the gate, drain and threshold voltage, respectively. Parameters will be further discuss in Section 2.3.3.

### 2.3.2 Operation Modes

Analogous to conventional MOSFETs, depending on whether the device requires a gate potential to be turned ON, OEETs exhibit two operation modes: depletion and enhancement (the latter often referred to as accumulation in the context of OEETs). The operation modes are closely linked to the nature of the channel material.

As illustrated in Figure 2.11A and B, the polymer can be either intrinsically doped (conductive) or undoped (insulating). In the first scenario, the OMIEC already possesses anions that induce charges within its backbone. Consequently, to turn off the device, cations need to be injected to counteract this effect. Conversely, for an insulating polymer channel, a zero-gate biased OEET will have no charges induced in its backbone, resulting in the OFF state. To transition to the ON state, a gate voltage is required to drive anions into the polymer and induce charges.

## 2. BACKGROUND

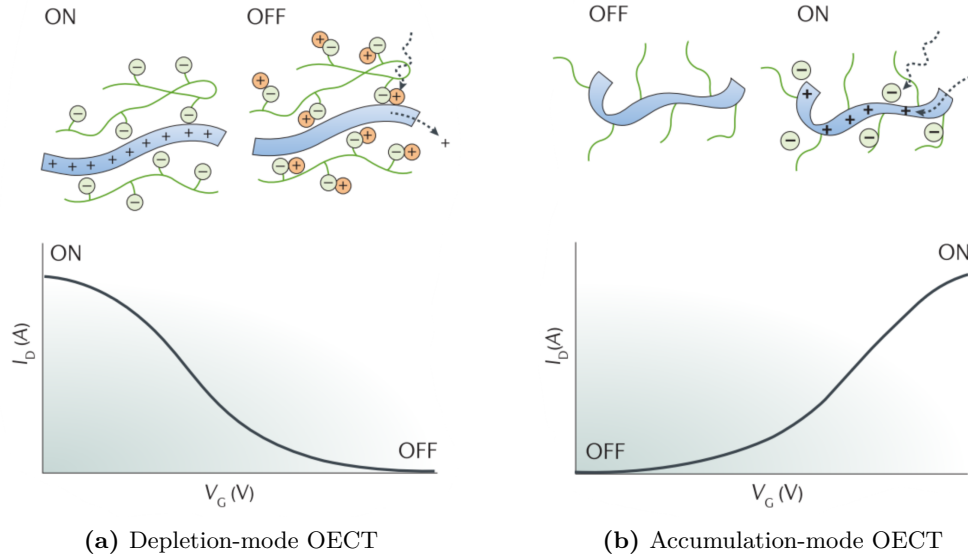


**Figure 2.11:** a) Transfer curve showing depletion-mode operation of a p-type OEET with a conducting polymer channel. b) Transfer curve showing accumulation-mode operation of a p-type OEET with a insulating polymer channel. Images extracted from reference [1].

### 2.3.2.1 Standard material for depletion-mode OECTs

Poly(3,4-ethylenedioxythiophene) poly(styrene-sulfonate) (PEDOT:PSS) is a “*degenerately doped*” [23] or conductive polymer that is widely used in various applications in organic electronics. Classified as type I OMIEC, as seen in Figure 2.6, it is a blend between a conjugated polymer (PEDOT) and a polyelectrolyte (PSS), the latter possesses chemically linked ions and serves as a polymeric acid template to allow dispersable suspensions [19].

Due to its commercial availability, operational stability, and relatively high performance, PEDOT:PSS became a standard material for p-type OECTs. However, its main drawback lies in its depletion-mode operation.

With the aim of minimizing power consumption, there is a strong interest in fabricating high-performance accumulation-mode devices [2][15][24][25]. These devices offer the advantage of dissipating less static power when the device is not in operation, due to low OFF current [16].

### 2.3.2.2 Prospective materials for accumulation-mode OECTs

PEDOT:PSS has not been ruled out as a possible accumulation-mode OECT, Keene et al. employed a series of amines to de-dope PEDOT:PSS and achieve OECTs with negative turn-on voltages [25]. However, synthetically modifying PEDOT:PSS in a controlled manner remains a challenge.

In parallel to these efforts, researchers are also working on the design of new conjugated polymers with the aim of not only having accumulation-mode OECTs but enhancing their performance. Nielsen et al. reported a series of semiconducting polymers with triethylene glycol (TEG) side chains, some of which demonstrated good performance. Among the five thiophene- and benzodithiophene-based polymers, they found out that the one with a backbone consisting of 2,2'-bithiophene (blue) polymerized with other thiophene molecule (green), named as **g2T-T**, as seen in Figure 2.12, exhibited the highest performance [2].

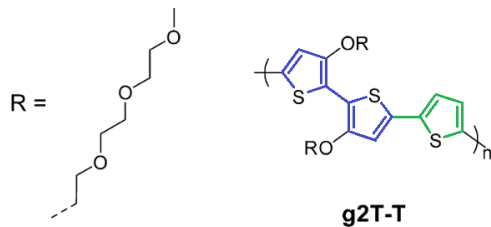


**Figure 2.12:** Chemical structure of polymer with backbone g2T-T, R representing the side chain. Extracted from reference [2].

Moser et al. conducted a study using the same backbone (g2T-T) to investigate the impact of the length of the ethylene glycol (EG) side chain on the performance of OECTs [26]. They found that reducing the side chain length maximized both the capacitance and mobility of the OECTs. However, a shorter side chain is less favorable for ion-polymer interaction.

Their research suggested an optimum-side-chain length of 3 monomers, compared to 2, 4 and 6 monomer. OECTs based on 3-(2-(2-methoxyethoxy)ethoxy) thiophene (p(g3T2-T)) exhibited a turn-on voltage close to zero and superior performance compared to other thiophene-based species (as seen in Figure 2.13 and Table 2.1), even surpassing PEDOT:PSS-based OECTs [24].

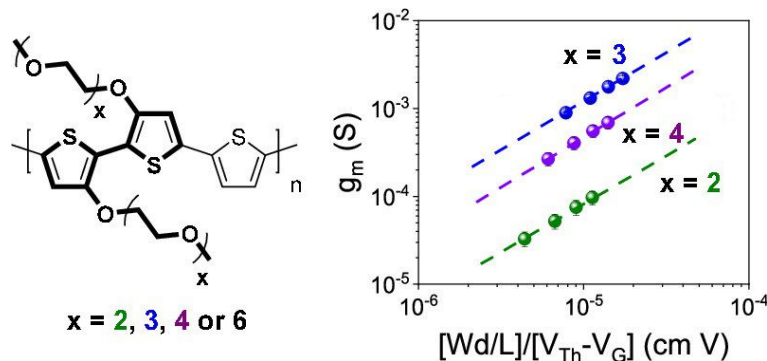


**Figure 2.13:** (Left) Chemical structure of the repeat units for p(gxT2-T). (Right) Transconductance vs channel geometry and operating parameters of p(gxT2-T) for  $x = 2, 3$  and  $4$ . Extracted from reference [26].

The structure of the polymer was designed to have a backbone that warrants

## 2. BACKGROUND

---

reversibility during electrochemical redox reactions and good electronic transport, while the side chains enhance its stability in aqueous electrolytes and facilitate efficient transport of both ionic and electronic charge carrier [27].

Under the classification presented in Figure 2.6, p(g3T2-T) can be categorized as a type VI OMIEC that consists of a conjugated polymer with ions introduced as free species. Whereas, PEDOT:PSS contains ions that are chemically linked to the polyelectrolyte (PSS). This structural distinction results in p(g3T2-T) displaying larger magnitudes of ionic-electronic coupling and volumetric capacitance compared to biphasic OMIECs like PEDOT:PSS [19]. Understanding these structural characteristics is crucial for addressing the challenges associated with achieving stable OEETs, as it will be further addressed in this thesis.

**Table 2.1:** Volumetric capacitance ( $C^*$ ) of OEETs channel materials including p(g2T2-T), p(g3T2-T), p(g4T2-T) and PEDOT:PSS using a 0.1 NaCl electrolyte and Ag/AgCl pellet electrode.

Polymer	$C^*$ ( $\text{Fcm}^{-3}$ )	Reference
p(g2T2-T)	8±2	[26]
p(g3T2-T)	211±18	[26]
p(g4T2-T)	192±10	[26]
PEDOT:PSS	39	[24]

### 2.3.3 Important Figures of Merit

#### 2.3.3.1 Transconductance

Transconductance is considered as the most important parameter for measuring the amplification capability of any transistor. It is calculated as the first-order derivative of the output current (drain current) with respect to the input voltage (gate-source voltage), expressed as  $g_m = \partial I_D / \partial V_{GS}$ . Bernards and Malliaras derived this parameter in their mathematical model for depletion-mode p-type OEETs [23], as discussed in Section 2.3.1. When considering both n-type and p-type OEETs, the transconductance can be expressed as follows:

$$g_m = \frac{Wd}{L} \mu C^* |(V_{th} - V_G)|, \quad (2.2)$$

where  $W$ ,  $L$  and  $d$  are the channel width, length, and thickness, respectively,  $\mu C^*$  denotes the product of mobility and volumetric capacitance, while  $V_G$  and  $V_{th}$  stand for the gate voltage and threshold voltage, which will be further discussed in the following subsections.

Typically, the maximum transconductance ( $g_{m,max}$ ) is reported, which falls into the saturation regime. Inal et al. reported the maximum transconductance for various channel materials with different device geometry parameters. They used an Ag/AgCl pellet as reference/gate electrode and 0.1M NaCl as electrolyte. Their results showed that OEETs with polymerized g2T backbones exhibited the best

performance, achieving transconductance values ranging from 1 to 30 mS, depending on the geometry (Figure 2.14A) [24].

### 2.3.3.2 $\mu C^*$ product

The parameter  $\mu C^*$  is considered the most important for benchmarking OEET channel materials because it represents both the ionic and electronic transport properties [24]. It is the product of two important parameters,  $\mu$ , the electronic mobility, and  $C^*$ , the volumetric capacitance, the latter encloses the ion penetration, transport, and storage ability of the OMIEC film.

Along with the transconductance, Inal et al. determined the values of  $\mu C^*$  by calculating the linear slope of the maximum transconductance and channel geometry (Figure 2.14A), using Equation 2.2. They correlated their results with independent calculations of both parameters and found that polymerized g2T backbones exhibited the highest  $\mu C^*$  value of  $261 \pm 29 \text{ F cm}^{-1} \text{ V}^{-1} \text{ s}^{-1}$ . Among the materials that showed a close 1:1 relationship for both methods of calculation of the  $\mu C^*$  product, polymerized g2T backbones stood out (Figure 2.14B) [24].

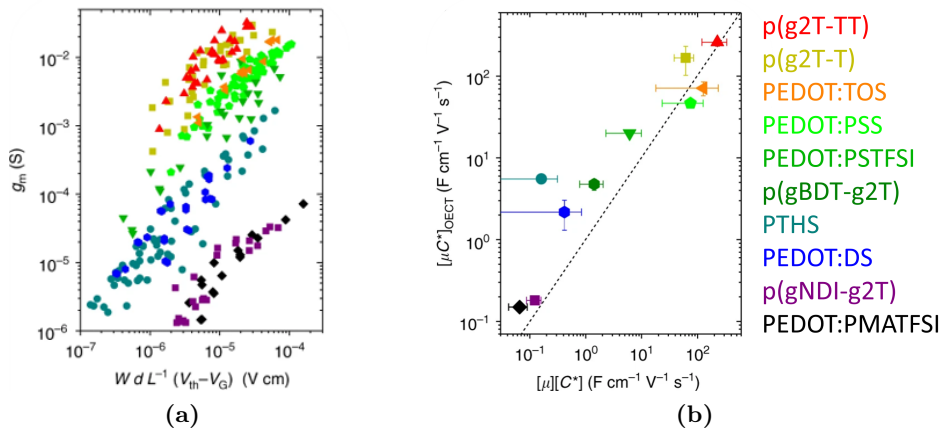


**Figure 2.14:** a) Plot of  $\mu C^*$  product calculated by the linear slope between transconductance and channel geometry. b) Calculated slope from a) in function of the product of independent determination of  $\mu$  and  $C^*$ , dotted line represents the 1:1 relation between both methods of calculation. Extracted from reference [24].

Calculating the electronic mobility ( $\mu$ ) independently is challenging due to the presence of ionic species. This calculation is normally performed in transient regimes, taking advantage of ions' lower mobility, but it is outside the scope of this work.

One method to calculate the volumetric capacitance ( $C^*$ ) is by performing Electrochemical Impedance Spectroscopy (EIS). Equation 2.3 is used to calculate the capacitance ( $C$ ) based on the imaginary part of impedance ( $Z^{img}$ ) at low frequency ranges where the capacitance should describe a plateau. The calculated capacitance is then divided by the film volume to obtain  $C^*$  [28].

## 2. BACKGROUND

---

$$C = \frac{1}{2\pi \cdot f \cdot |Z^{img}|}, \quad (2.3)$$

It is important to note that the capacitance ( $C$ ) can be potential-dependent when electrochemical doping is modulated in OECTs with an applied bias [24].

### 2.3.3.3 Threshold voltage

The threshold voltage ( $V_{th}$ ) in an OECT can be determined from the steady-state transfer characteristics ( $I_D$  vs  $V_{GS}$ ). To calculate  $V_{th}$ , you can plot the square root of  $I_D$  as a function of  $V_{GS}$  and extrapolate the linear portion of the slope, where it intersects the x-axis. This value of  $V_{th}$  represents the “film’s readiness for ion penetration” in OECTs [28].

Controlling or shifting the threshold voltage is desirable, specially for integrating transistors into circuits to meet specific requirements for operation, noise margins, and power consumption. There are different approaches to achieve this. One approach is the chemical de-doping of PEDOT:PSS, as discussed in previous sections, which can shift the threshold voltage to negative values characteristic of accumulation-mode OECTs [25].

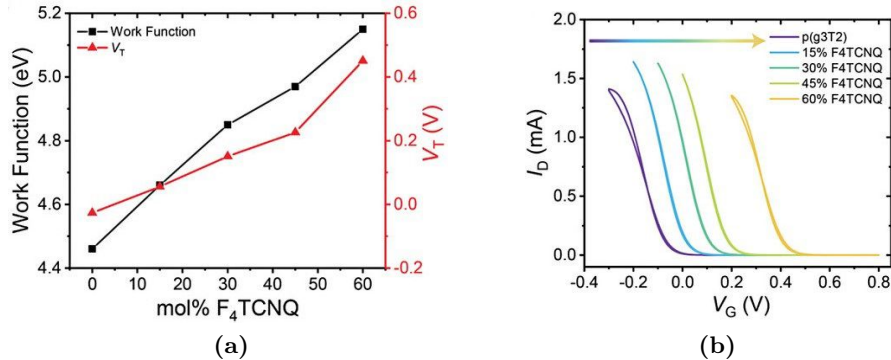


**Figure 2.15:** Controlling OECT threshold voltage by chemical doping of p(g3T2-T) gate electrode with  $F_4TCNQ$ . a) Plot of threshold voltage and gate work function for doped gates of different dopant concentrations. b) Transfer curves of p(g3T2-T) channel OECT with p(g3T2-T) gates of various  $F_4TCNQ$  dopant concentrations. Extracted from reference [3].

Another approach, explored by Tan et al., involves tuning the doping level of the gate to shift the threshold voltage. They used p(g3T2-T) and achieved a 400 mV change in threshold voltage with a 60% molar ratio of  $F_4TCNQ$  dopant, as shown in Figure 2.15. This approach offers advantages such as i) protecting the material from oxidation by bringing the Fermi level towards the highest occupied molecular orbital, and ii) avoiding interference with the channel which helps to maintain the transconductance unaffected [3].

### 2.3.4 Side Reactions

#### 2.3.4.1 Water uptake and swelling

Water uptake and swelling are important side reactions that occur when OMIECs come into contact with water-based electrolytes. Even in the pursuit of solid-state OECTs, precursors may contain a certain degree of water content [4][29], making it necessary to understand the impact of water-related side reactions.

Water uptake in OMIECs causes their increase of mass (swelling) and changes in morphology. This water uptake occurs because OMIECs need to compensate for their intrinsic doping, and as a result, “*the effect of doping-induced hydration on the OMIEC morphology must be taken into account when designing OECTs*” [30].

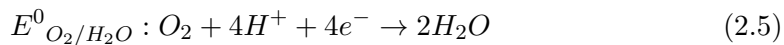
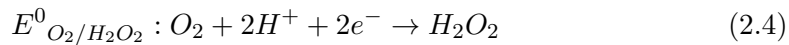
Savva et al. conducted a study to investigate the influence of water on the performance of PEDOT:PSS OECTs. They found that water uptake led to a 10-13% increase in mass under non-biased conditions. Interestingly, the concentration of water played a role in the ionic charging rate. While lower concentrations of water ( $\text{NaCl}_{aq}$  10 mM, 100mM, 1M, and 6M) led to faster ionic charging, the fastest response time was achieved with  $\text{NaCl}_{aq}$  1 M. This was attributed to attractive forces between counter ions, which hindered the drift of anions and delayed the injection of ions from the electrolyte [31].

Another study by Savva et al. showed that a certain level of hydration is necessary for facile ionic transport, but can have a negative impact on electronic charge transport, particularly in glycol-based side chains [30]. These side chains are commonly used in accumulation-mode OECTs, where ionic transport is already enhanced through side-chain engineering [27].

#### 2.3.4.2 Oxygen Reduction Reaction (ORR)

The Oxygen Reduction Reaction (ORR) is a common undesirable side reaction that occurs under environmental conditions, especially in devices fabricated with polymers having low ionization potential (IPs). The use of OMIECs with low IPs is frequent in accumulation-mode OECTs.

The ORR is a non-capacitive faradaic reaction that takes place between the OMIEC and molecular oxygen, involving electron-transfer. This reaction can yield either hydrogen peroxide ( $\text{H}_2\text{O}_2$ ) or water ( $\text{H}_2\text{O}$ ), as described in 2.4 and 2.5, or it can result in the oxidation (p-doping) of the OMIEC which acts as the catalyst [16].



As represented in Figure 2.16,  $\eta_1$  and  $\eta_2$  represent the free energy difference between reactants and the reaction products  $\text{H}_2\text{O}_2$  and  $\text{H}_2\text{O}$ , respectively. If this free energy difference is negative, indicating that the reaction requires an energy input, the ORR is endergonic, while a positive free energy difference makes it exergonic

## 2. BACKGROUND

---

(spontaneous). For instance, to prevent the formation of oxygen peroxide, a polymer with higher IP ( $> 4.9\text{eV}$ ) would be required.

In the context of OECTs, where polymers like PEDOT:PSS and p(g3T2-T) are used, it is important to recognize that these materials exhibit exergonic reactions under environmental conditions. Therefore, it is crucial to consider the impact of the ORR on device stability and performance, particularly in applications where long-term reliability is essential.

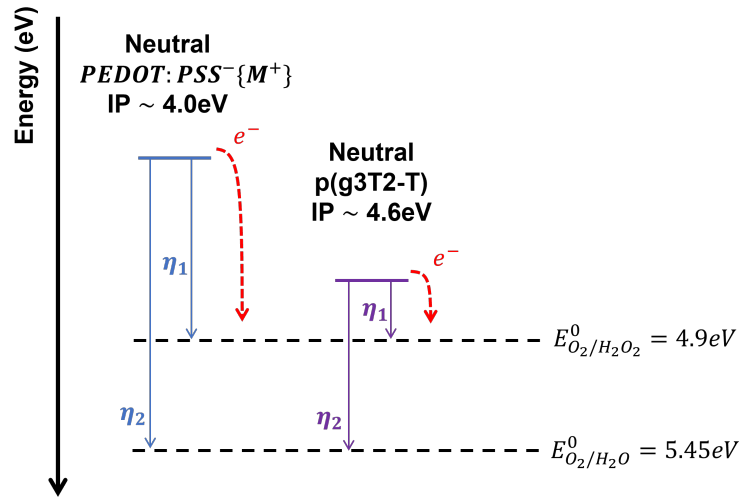


**Figure 2.16:** Simplified mechanism of two- and four-electron Oxygen Reduction Reactions with neutral states of OMIECs: p(g3T2-T) and PEDOT:PSS. The free energy difference between reactant and the reaction products is represented by  $\eta$ . Image adapted from reference [16], where values are defined from cyclic voltammetry measurements using Ag/AgCl as reference electrode and NaCl as electrolyte.

# Chapter 3

## Experimental Methods

### 3.1 Materials

All reactives were purchased from commercial suppliers.

- Chromium etchant: High purity ceric ammonium nitrate, Standard, Sigma Aldrich
- Gold etchant: HHPAA (2-Hydroxy-4'-(2-hydroxyethoxy)-2-methylpropiophenone), 98%, Standard, Sigma Aldrich
- Developer: AZ 726 MIF Developer, Merck performance Materials GmbH
- EG: Ethylene glycol,  $\geq$  95%, Sigma Aldrich
- [EMIM][EtSO<sub>4</sub>]: (1-Ethyl-3-methylimidazolium ethyl sulfate),  $\geq$ 95%, Sigma Aldrich
- MBBAm: (N,N'-Methylenebisacrylamide), 99%, Sigma Aldrich
- NIPAm: (N-Isopropylacrylamide), 97%, Alfa Aesar
- Sacrificial Layer 1: Sacrificial Layer 1 (SL1), Orthogonal Inc
- Photoresist: AZ 1518 Photoresist, Merck Performance Materials GmbH & Microchemical GmbH
- Photoresist for undoped species: NLOF 2020, commercial negative-tone photoresist, Microchemical
- Orthogonal Photoresist for doped species: OSCoR 4020 Photoresist, Orthogonal Inc.
- Developer for SL1: Developer HF 7300, Orthogonal Inc.
- Orthogonal Developer for OSCor 4020: Orthogonal Developer 103a, Orthogonal Inc.

### 3. EXPERIMENTAL METHODS

---

- Orthogonal Stripper: Orthogonal Stripper 900, Orthogonal Inc.
- p(g3T2-T): 3-(2-(2-methoxyethoxy)ethoxy)thiophene from Professor Iain McCulloch, Chemistry Research Laboratory, University of Oxford.
- Dopants: 1,3,4,5,7,8-hexafluorotetracyanonaphthoquinodimethane ( $F_6\text{TCNNQ}$ ) and 1,3,4,5-tetrafluorotetracyanonaphthoquinodimethane ( $F_4\text{TCNQ}$ ), 97%, Sigma Aldrich.
- Adhesion promoter: Silane A174 (3-(Trimethoxysilyl)propyl methacrylate), TCI.

## 3.2 Equipment

- Baking: All baking steps were carried out on a Stuart SD160 digital hotplate (Stuart Equipment, UK).
- Electrical characterization (ambient): Device characterization under ambient conditions was performed on a Everbeing C-6 Probe Station (Everbeing Int'l Corp., Taiwan), connected to a Keithley 4200-SCS Semiconductor Characterisation System (Keithley Instruments, USA).
- Electrical characterization (glovebox): Device characterization was performed in a nitrogen-filled glovebox. Probing needles were connected to two Keithley 236 Source Measure Units (Keithley Instruments, USA).
- Cyclic voltammetry and Impedance measurements: Measurements were carried out by using a Metrohm Autolab PGSTAT302N potentiostat/galvanostat (Metrohm AG, Switzerland).
- Micrographs: Micrographs were taken on a Nikon Eclipse LV100ND microscope, equipped with a DS-Fi2 camera (Nikon, Japan).
- Photolithography: Photolithography was carried out on a SÜSS Microtec MJB4 maskaligner system (SÜSS Microtec AG, Germany).
- Photomasks: Photomasks were custom made by Compugraphics Jena in a 4-inch format (soda-lime glass covered with chromium) and held several mask designs (Compugraphics Jena GmbH, Germany).
- Plasma cleaning:  $O_2$ -plasma cleaning was performed by using a Harrick PDC-002 plasma cleaner (Harrick Plasma, USA), connected to a Leybold Heraeus Combitron CM 330 Vacuum Gauge Controller (Leybold GmbH, Germany).
- Plasma etching:  $O_2$ -plasma etching was performed by using a Diener electronic ATTO plasma cleaner (Diener electronic GmbH & Co. KG, Germany).
- Profilometry: Profilometry was performed on a Veeco Dektak 150 surface profiler (Veeco Instruments Inc., USA).

- Film resistance measurements: The film resistance was measured using a linear four-point probe system (Lucas four-point probe connector) connected to a multimeter (Keithley 2010 Multimeter).
- Transmittance and Reflectance measurements: Measurements were performed with UV-Visible-NearInfraRed Spectroscopy on a SolidSpec-3700 UV-Vis-NIR spectrometer using an integral sphere from Shimadzu.
- Energy of HOMO/HBEC cutoff measurements: Measurements were done using Ultraviolet Photoelectron Spectroscopy (UPS) on a PHOIBOS 100 from Specs, a Helium plasma discharge lamp (UVS10/35, Specs).
- Spincoating: Samples were coated with a SAWATEC SM-180-BT spincoater (SAWATEC AG, Switzerland).

### 3.3 Software

- Data processing: All data was processed by customized scripts written in Python. Files import and manipulation was done by using OS [32] and CSV [33] modules. Mathematical computations (e.g. fits, integration) were carried out by employing the NumPy [34], SciPy [35], and PeakDetect [36] libraries. Visualisations were performed using the Matplotlib library [37]. All is compiled in the following GitHub Repository: **marivelasco25/Thesis.git**.
- Electrical characterization: Measurements were performed by controlling SMUs through the in-house developed SweepMe! software (<https://sweep-me.net/>).
- Profilometry: Profilometry was performed by using the Dektak software (Veeco Instruments Inc., USA).
- Cyclic voltammetry: Measurements were performed by using the NOVA software (Metrohm AG, Switzerland). Parameters were fixed and are described in the following table:

**Table 3.1:** Cyclic Voltammetry parameters.

Parameter	Value
Start/Stop potential	0 V
Upper vertex potential	1 V
Lower vertex potential	-1 V
Number of scans	10
Scan rate	0.1 V/s

- Impedance measurements: Measurements were performed by using the NOVA software (Metrohm AG, Switzerland) in potentiostatic mode. Parameters were fixed and are described in the following table:

### 3. EXPERIMENTAL METHODS

---

**Table 3.2:** Electrochemical Impedance Spectroscopy parameters.

Parameter	Value
Initial frequency	$10^5$ Hz
Final frequency	$10^{-1}$ Hz
Frequencies per decade	10
Amplitude ( $V_{RMS}$ )	0.01 V

## 3.4 Photomask

The employed photolithography mask for OECT fabrication depict a specific layout of gold electrodes, as illustrated in Figure 3.1. Detailed information about the photolithography process is provided in the following section.

This layout accommodates 14 devices, each with a channel length of 70  $\mu\text{m}$  and a 20  $\mu\text{m}$  overlap on both sides. The channel width is set at 190  $\mu\text{m}$ . Additionally, the gate electrode dimensions describes a length of 190  $\mu\text{m}$  and a width of 220  $\mu\text{m}$ , with a gate-channel distance of 30  $\mu\text{m}$ . All 14 devices will be located within a glass sample substrate measuring  $2.5 \times 2.5 \text{ cm}^2$ .

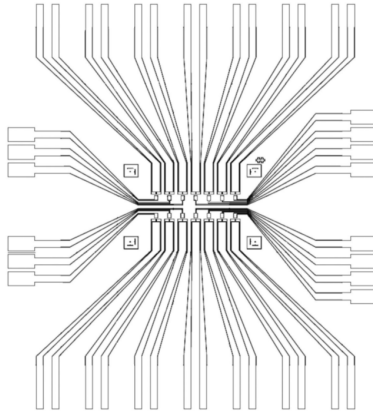


**Figure 3.1:** Used photomask for fabricated OECT gold electrodes.

## 3.5 Experimental Procedure

All fabrication steps were performed under standard cleanroom conditions.

### 3.5.1 Preparation of Films

**Dynamic spin-coating of p(g3T2-T).** In contrast to the approach described in reference [3], which employed drop-casting for the deposition of undoped and doped p(g3T2-T) films, our objective is to enable photolithography and facilitate a miniaturization process. To achieve this, uniform films are needed. The BioSens group members at IAPP had previously established dynamic spin-coating method

### 3.5. Experimental Procedure

due to the high volatility of p(g3T2-T) solvent, chloroform. Substrates were cleaned through sequential steps of ultrasonic bath in acetone for 15 minutes, IPA rinse, N<sub>2</sub> drying, and 5 minutes of O<sub>2</sub> plasma etching (0.3 mbar). Then, 70 $\mu$ L of 10 mg/mL of p(g3T2-T) mixed at 60°C for 20 minutes, was applied using dynamic spin-coating at 3000 RPM for 60s, yielding approximately 70nm thick films. The samples were then dried at 80°C.

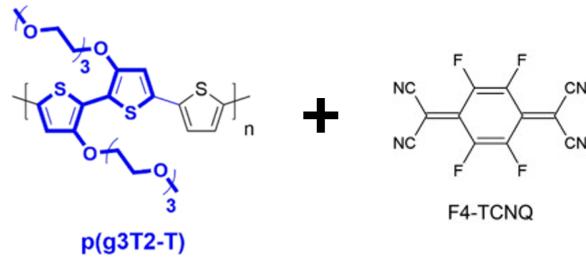


**Figure 3.2:** Chemical structures of the repeat units of p(g3T2-T) and F<sub>4</sub>TCNQ dopant.

**Dynamic spin-coating of F<sub>4</sub>TCNQ dopant.** Different doping levels of p(g3T2-T) were achieved by dynamic spin-coating 140 $\mu$ L of dopants at different concentrations (5, 10 and 20 mg/mL, as seen in Figure 3.3), previously mixed in acetonitrile at 60°C for 20 minutes. The samples were then dried at 80°C.

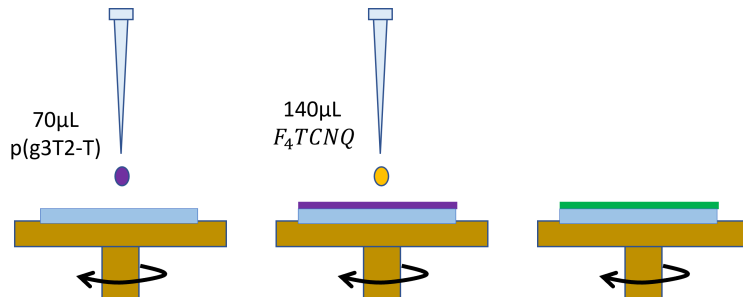


**Figure 3.3:** Dynamic spin-coating process to obtain undoped and doped films of p(g3T2-T)).

#### 3.5.2 Doping Characterization of Films

**Profilometer.** The films were scratched 4 times to remove part of material, and measure the cavity depth to obtain the film thickness.

**Four-point probe.** Sheet resistance and resistivity were calculated following reference [38], via equations:

### 3. EXPERIMENTAL METHODS

---

$$R_s = \frac{\pi}{\ln(2)} R = 4,53R \quad [\Omega/sq], \quad (3.1)$$

where R is the resistance measured with the four-point probe setup, and

$$\rho = R_s t \quad [\Omega.cm], \quad (3.2)$$

where  $t$  is the thickness of the film.

**UV-Vis-NIR Spectroscopy.** After the preparation of the films onto quartz substrates, transmittance (T) and reflectance (R) was measured using the UV-Vis-NIR Spectrometer in the range of 285 to 1600 nm. Then, absorption (A) was calculated via

$$A = 1 - T - R, \quad (3.3)$$

and normalized with respect to the incoming light [39]. Additional measurements were taken, after some days of storage under ambient conditions to check its stability in air.

**Ultraviolet Photoelectron Spectroscopy.** After the preparation of the films, the energy of the highest occupied molecular orbital cutoff ( $E_{HOMO}$ ) and the high binding energy cutoff  $E_{HBEC}$  was measuring using UPS. The pressure in the chamber during measurements was about  $5 \cdot 10^{-9}$  mbar, while the base pressure is in the range of  $10 \cdot 10^{-10}$  mbar. The workfunction (WF) and ionization energy (IE) are calculated by using the following equations:

$$WF = h\nu - E_{HBEC} \quad [eV], \quad (3.4)$$

$$IE = h\nu - (E_{HBEC} - E_{HOMO}) \quad [eV], \quad (3.5)$$

where  $h\nu = 21.22eV$ , the main He I excitation line of the Helium plasma discharge lamp [40].

#### 3.5.3 Fabrication of Organic Electrochemical Transistors

Photolithographically patterned substrates with gold contacts for source, drain and gate were obtained using mask layout illustrated in Figure 3.1. The steps outlined in references [4] and [41] were followed, which is also represented in Figure 3.4.

Then p(g3T2-T) films were deposited following the procedure described in the previous section. The patterning of doped-p(g3T2-T) channel adopted a procedure similar to the one described in references [4][41], which involves the use of PEDOT:PSS. However, some modifications in the exposure and developing times were made. In contrast, the patterning of undoped-p(g3T2-T) samples, required a different protocol. A sacrificial layer is introduced to ensure proper cross-linking with photoresist. Both processes are detailed in the following:

### 3.5. Experimental Procedure

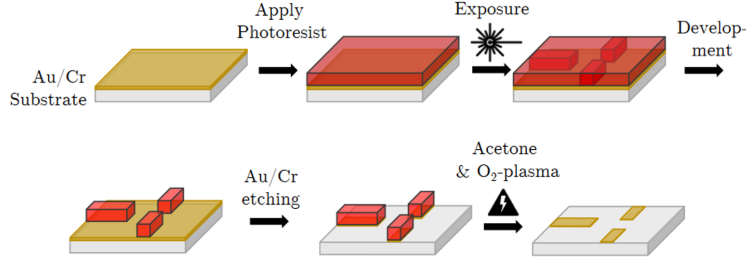


**Figure 3.4:** Visualization of the workflow for Au-contacts patterning. Image modified based on reference [41].

**Patterning undoped-p(g3T2-T).** Patterning of the p(g3T2-T) was achieved with photolithography, as shown in Figure 3.5. First, a fluoropolymer Sacrificial Layer 1 (SL1) was spin-coated at 6000 RPM for 60 s, followed by a baking step for 180 s at 113°C. Before the deposition of photoresist, a O<sub>2</sub> plasma cleaning step was applied for 60 s to promote adhesion. Then, NLOF 2020 photoresist was spin-coated at 3000 RPM for 60 s and baked for another 60 s at 113°C. Exposure of negative resist was performed for 12 s by shadowing all areas except the ones of interest. After post-baking for 60 s at 113°C, NLOF was developed by rinsing the sample in AZ MIF 726 for 20 s and wash off in DI water (carried out extra times if necessary). Next, SL1 was developed using HF 7300 developer for 45 s and spin rinsed at 3000 RPM (carried out extra times if necessary). Excess of p(g3T2-T) was removed by O<sub>2</sub>-plasma etching for 180 s. The sample was placed in Orthogonal Stripper 900 overnight at room temperature, to complete the removal. Finally, ultrasonication in acetone was added for 15 min the next day.

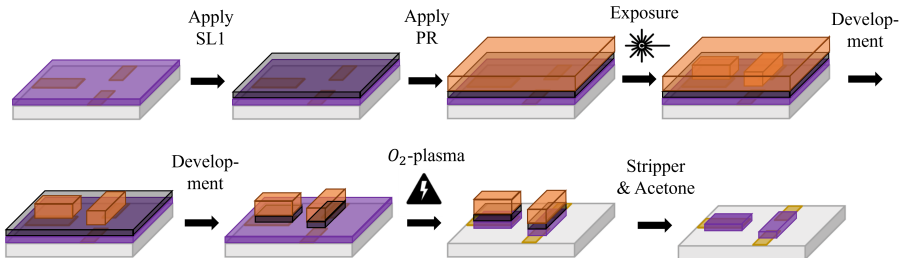


**Figure 3.5:** Visualization of the workflow for patterning undoped p(g3T2-T).

**Patterning doped-p(g3T2-T).** Patterning of the doped-p(g3T2-T) was achieved with photolithography, as shown in Figure 3.6. First, the orthogonal photoresist OSCoR 4020 was spin coated at 3000 RPM for 60 s and baked for another 60 s at 103°C. Exposure of negative resist was performed for 20 s with shadowing all areas except the ones of interest, one extra cycle was added if using higher dopant concentration (10 mg/mL). After post-baking for 60 s at 103°C, OSCoR was

### 3. EXPERIMENTAL METHODS

---

developed using Orthogonal Developer 103a for 45 s and spin rinsed at 3000 RPM for 60 s (carried out extra times if necessary). Excess of doped-p(g3T2-T) was removed by O<sub>2</sub>-plasma etching for 180 s. The sample was placed in Orthogonal Stripper 900 overnight at room temperature.

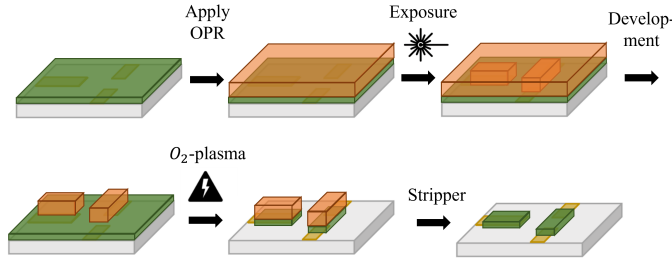


**Figure 3.6:** Visualization of the workflow for patterning doped p(g3T2-T).

#### 3.5.3.1 Influence of Doping on OEET Channel

**OEET with undoped- and doped-p(g3T2-T) channel.** A solid-state electrolyte precursor was prepared according to the details provided in Table 3.3. Next, 20 $\mu$ L of this precursor were drop-casted to the patterned samples, both undoped and doped, covering all 14 devices in the sample. Finally, a Ag/AgCl pellet was installed and used as gate (Figure 3.7). Transfer characteristics were measured under ambient conditions with a  $V_{GS}$  swept backwards from 1.0 V to -0.8 V.

**Table 3.3:** Composition of the solid-state electrolyte [4].

Component	Amount	Function
H <sub>2</sub> O	1.0 mL	dilution
[EMIM][EtSO <sub>4</sub> ]	1.5 mL	ionic liquid
MBBAm	20 mg	crosslinker
NIPAm	750 mg	monomer
HPAA	200 mg	photoinitiator
EG	1.5 mL	increase viscosity, ensures good print
Triton	1 drop	surfactant, ensures good print

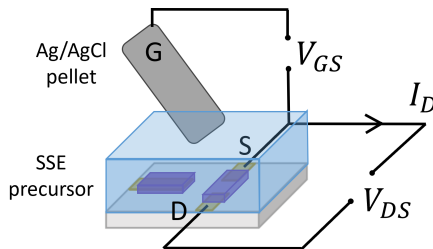


**Figure 3.7:** Representation of experimental setup for measuring threshold voltage shift of a single OEET under ambient conditions. Scheme is not drawn to scale.

### 3.5.3.2 Stability on Air of p(g3T2-T)

In this subsection, stability tests were conducted on both undoped and doped p(g3T2-T) samples. These samples were doped with F<sub>6</sub>TCNNQ, following same procedure described in subsection 3.5.1. The channel conductivity was measured before and after patterning and after contact with SSE while a fixed biased drain-source voltage was maintained, under N<sub>2</sub> and ambient conditions.

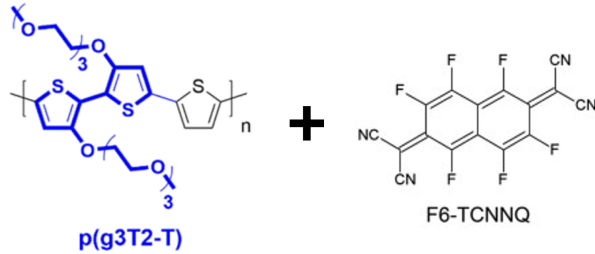


**Figure 3.8:** Chemical structures of the repeat units of p(g3T2-T) and F<sub>6</sub>TCNNQ dopant.

**Channel conductivity measurements.** Undoped-p(g3T2-T) sample was measured in N<sub>2</sub> then ambient conditions immediately after spin-coating onto substrate with patterned gold contacts. Then, sample was measured after patterning process (as described in previous section). Finally, upon drop-casting solid-state electrolyte precursor. The doped-p(g3T2-T) channel was measured after patterning and upon drop-casting solid-state electrolyte precursor.

### 3.5.3.3 Reverse Oxidation of Undoped-p(g3T2-T)

**By electrochemical dedoping.** Undoped-p(g3T2-T) samples onto patterned-gold-contacts substrates were prepared. The solid-state-electrolyte precursor was dropcast onto the 14 devices, one device source-drain was negatively-biased and applied a positive gate voltage. Channel conductivity was monitored. Finally, other devices on the sample were measured to detect any effect of the process.

**By heating.** An undoped-p(g3T2-T) solid-OECT, whose fabrication will be described in the following subsection 3.5.3.4, was exposed to ambient conditions, devices were clearly oxidized. The sample was placed on a hot plate at 120°C, brought back to glovebox, and measured the following day.

### 3.5.3.4 Solid-OECTs using Undoped-p(g3T2-T)

After following the patterning steps for undoped-p(g3T2-T) from Subsection 3.5.3.1. Three different methods of applying the solid-state electrolyte precursor were tested. Then, transfer characteristics were measured at a constant V<sub>DS</sub> of -0.1V, and a V<sub>GS</sub> swept backwards from 1.0 V to 1.0 V at a scanning rate of 0.083 V/s. Cyclic

### 3. EXPERIMENTAL METHODS

---

voltammetry and electrochemical impedance spectroscopy were performed by short-circuiting source and drain to probe between channel and gate. Parameters were fixed as described in Section 3.3, and measurements were taken one day after the fabrication.

**Application of adhesion promoter.** An adhesion promoter, consisting of reactants detailed in Table 3.4, was applied to the substrate. The sample was placed in a Petri dish at 50°C and covered for 20 min. Subsequently, it was thoroughly rinse with ethanol and dried on a hot plate at 100°C for a minimum of 10 min. The composition and application steps of adhesion promoter was previously established by Biosens group members at IAPP.

**Table 3.4:** Composition of adhesion promoter.

Component	Amount
SilaneA174	30 $\mu$ L
Etolol	3mL
Acetic acid	60 $\mu$ L

**OECT with drop-casted Solid-State Electrolyte.** Solid-state electrolyte precursor was drop-casted and then exposed for 2 cycles of 60 s in a mask aligner, as shown in Figure 3.9A. No adhesion promoter was applied in this sample.

**OECT with photopatternable Solid-State Electrolyte.** After the application of the adhesion promoter, the solid-state electrolyte precursor was drop-casted onto the sample, followed by the placement of a Teflon foil to prevent contact with the mask, which would shadow all areas except the ones of interest in the negative resist. The sample was then exposed for 2 cycles of 60 s in a mask aligner. Removal of excess, non-cross-linked precursor was careful blown off with a N<sub>2</sub> gun, as shown in Figure 3.9B, following references [4][41].

**OECT with inkjet-printed Solid-State Electrolyte.** After the application of the adhesion promoter, the solid-state-electrolyte precursor was ink-jet printed and expose for 2 cycles of 60 s in mask aligner, as illustrated in Figure 3.9C. Parameters and procedure for ink-jet printing was previously established by members of BioSens group at IAPP.

#### 3.5.3.5 Solid-OECTs using Doped-p(g3T2-T)

**OECT with inkjet-printed Solid-State Electrolyte.** After the deposition of films and dopant (F<sub>6</sub>TCNNQ), films were stored in glovebox over the weekend to let dopants soak and dry. Then, the patterning steps for doped-p(g3T2-T) from Subsection 3.5.3.1 were followed with no extra cycles in exposure times. Solid-state electrolyte precursor was ink-jet printed as described in the previous subsection.

### 3.5. Experimental Procedure

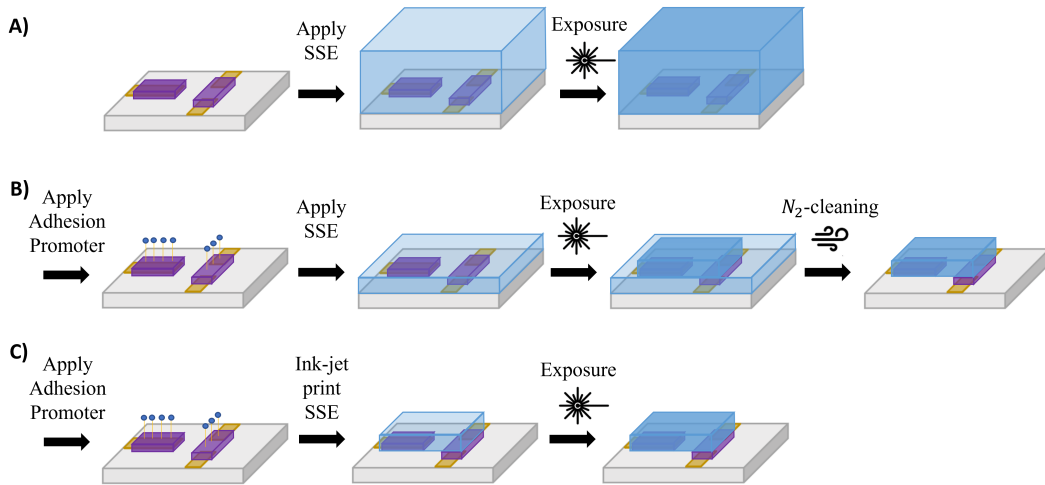


**Figure 3.9:** Visualization of the workflow for solid-OECT fabrication with undoped p(g3T2-T) by A) drop-casting SSE, B) photopatterning SSE, C) ink-jet printing SSE.

Then, transfer characteristics were measured at a constant  $V_{DS}$  of -0.1V, and a  $V_{GS}$  swept backwards from 1.0 V to 1.0 V at a scanning rate of 0.083 V/s. Cyclic voltammetry and electrochemical impedance spectroscopy were performed by short-circuiting source and drain to probe between channel and gate. Parameters were fixed as described in Section 3.3, and measurements were taken one day after the fabrication.

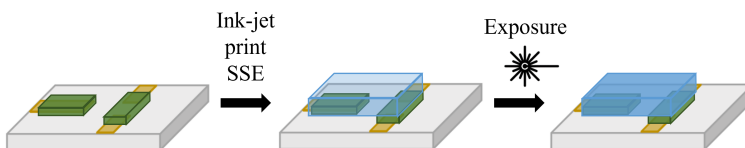


**Figure 3.10:** Visualization of the workflow for solid-OECT fabrication with doped p(g3T2-T) by ink-jet printing SSE.



# Chapter 4

## Results and Discussion

### 4.1 Doping Characterization

Upon increasing the dopant concentration deposited on top of the p(g3T2-T) film and subsequent baking, the reflection hue, as depicted in Figure 4.1 shift toward more yellowish tones.

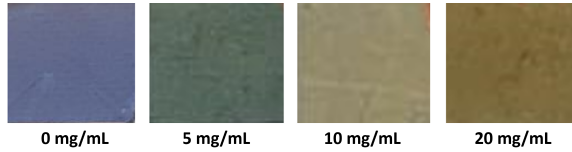


**Figure 4.1:** Color change upon increasing dopant concentration from 0 to 20 mg/mL.

#### 4.1.1 Thickness, Sheet Resistance and Resistivity

Sheet resistance and resistivity, as shown in Table 4.1, were calculated using equations 3.1 and 3.2, respectively, as described in previous chapter. The film thickness was determined through profilometer measurements, resulting in an approximate thickness of 70 nm.

**Table 4.1:** Sheet resistance and resistivity values for undoped and doped films of p(g3T2-T)

	Undoped	5 mg/mL	10 mg/mL	20 mg/mL
$R_S$ ( $\Omega/\text{sq}$ )	6.3M	104.6k	70.7k	49.4k
$\rho$ ( $\Omega\text{cm}$ )	44.1	0.73	0.49	0.35

Upon doping, a substantial decrease is observed in both sheet resistance and resistivity. However, this decrease is not as pronounced when higher dopant levels are introduced, as depicted in Figure 4.2. Nevertheless, when comparing the decrease

## 4. RESULTS AND DISCUSSION

---

among doped samples, a clear linear relationship becomes apparent with increasing the dopant concentration.

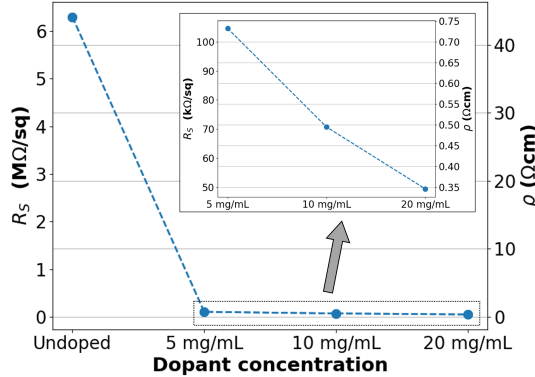


**Figure 4.2:** Sheet resistance and resistivity drop upon doping of p(g3T2-T). Inset represents the quasi-linear drop of parameters as between doped samples.

### 4.1.2 Absorbance and Dopants Diffusion

The visible color hue shift can be quasi-quantitatively described by examining the absorbance spectra of the samples, as illustrated in Figure 4.3. In the case of undoped-p(g3T2-T), there is a prominent absorption peak at 588 nm (red), which diminishes with increasing doping concentration, indicative of oxidation. Notably, new absorption peaks emerge at around 860 nm, a consequence of polaron generation, leading to new optical transitions, as explained in Chapter 2, Section 2.1.2.

Tan et al. documented the appearance of new absorption peaks within the 300 to 600 nm range. The higher energy (lower wavelength) peak is generated by unreacted neutral dopant species ( $\text{TCNQ}^0$ ), while the second is attributed to the new dopant anions ( $\text{TCNQ}^-$ ), which induce charges in our polymer [3]. Additionally, it is worth noting that, after several days of storage, the initially dominant peak of unreacted neutral dopants diminishes in intensity relative to the anions peak. This observation suggests ongoing diffusion of dopants through the polymer over time.

Absorbance values are directly correlated with the density of states of these new optical transitions [11]. In our spectra, the absorbance value at 860 nm of the lowest-doped p(g3T2-T) sample (5 mg/mL) is relatively higher, around 40%. This might initially appear counterintuitive. However, as the doping concentration increases, the formation of bipolarons and bipolaron bands becomes energetically more favorable [42]. This phenomenon aligns with observations in the higher wavelengths, such as at 1600 nm, where absorbance increases in the more highly doped p(g3T2-T) sample.

Moreover, Tan et al. reported the formation of bipolaron in this specific context, evidenced by a shift to lower energies in the broad absorbance spectrum within the mid-IR region (wavenumbers  $1000\text{-}1600\text{ cm}^{-1}$ ) [3]. Consequently, further analysis of hole bipolaron formation can be conducted with Fourier Transform InfraRed (FTIR) spectroscopy.

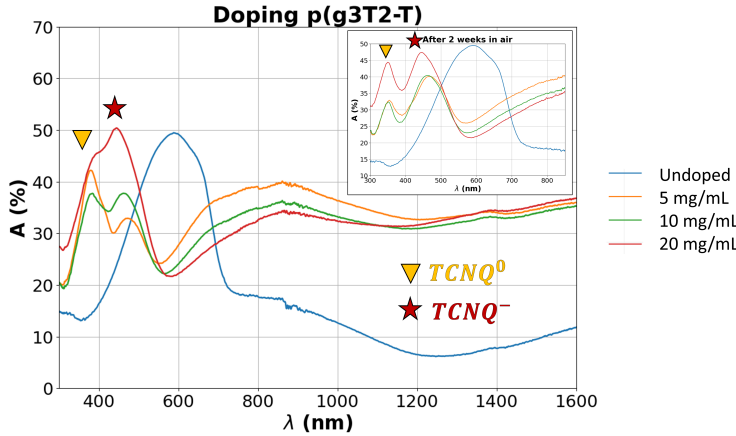


**Figure 4.3:** Spectra of undoped and doped-p(g3T2-T) at different doping levels, corresponding to samples on Figure 4.1. Inset represents absorbance after two weeks of storage in ambient conditions.

#### 4.1.3 Workfunction

In the context of studying electron energy levels in Ultraviolet Photoelectron Spectroscopy (UPS), the ideal film preparation involves working under inert conditions to prevent contamination. However, our current OECT fabrication process unavoidably exposes our films to ambient conditions. Consequently, we conducted measurements following deposition under these ambient conditions. As expected, we observed an increase in the workfunction, as evidenced by a shift in the Fermi level of the polymer. This shift towards the HOMO level becomes more pronounced at higher dopant concentrations, as depicted in Figure 4.4, which is characteristic of p-type doping. Unfortunately, potential contamination issues prevented the measurement of samples with a dopant concentration of 20 mg/mL, but the trend is clearly discernable.

**Table 4.2:** Calculated workfunction from UPS measurements and represented in Figure 4.4.

	Undoped	5 mg/mL	10 mg/mL
$E_{HBEC}$ [eV]	17.35	16.47	16.36
$E_{HOMO}$ (vs $E_F$ )	4.28	3.27	3.24
WF [eV]	3.87	4.28	4.86

It is crucial to recognize that UPS is a surface-sensitive measurement. The penetration depth of the ultraviolet-range photons in UPS is limited to approximately 2 nm, significantly less than the thickness of our polymer film (approximately 70 nm). Consequently, this technique restricts our understanding of the diffusion of dopants throughout the entire volume of the polymer. Although, we gained some insights into this matter in the previous subsection, further analysis could be carried out using X-Ray Photoelectron Spectroscopy, which offers a depth profiling mode.

#### 4. RESULTS AND DISCUSSION

---

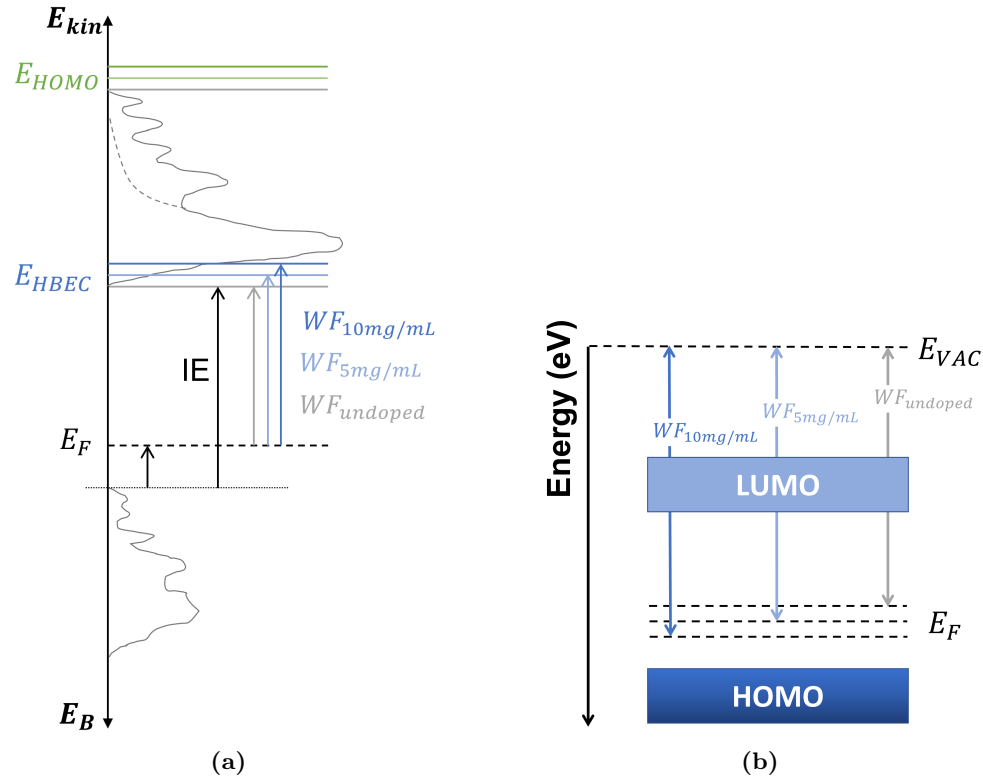


**Figure 4.4:** Graphical representation of a) the relationship between the binding energies  $E_B$  and the kinetic energy of the photoelectrons  $E_{kin}$ , and b) the Fermi level shift, upon doping.

## 4.2 Fabrication of Organic Electrochemical Transistors

The patterning process was successfully accomplished via photolithography, as detailed in Chapter 3 Section 3.5.3.1, employing a mask that included a microstructured gate. This setup is ideal for studying OECTs with both channel and gate constructed from the same OMIEC material, commonly PEDOT:PSS. The result of this process is displayed in Figure 4.5.

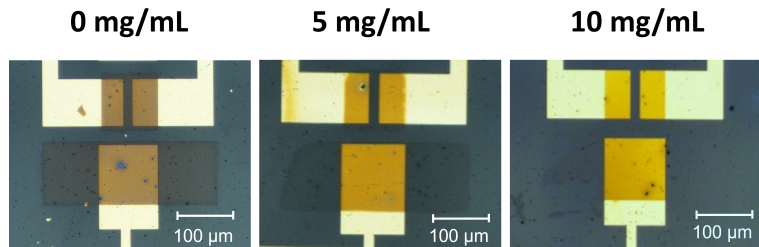


**Figure 4.5:** Micrographs of patterned channel and gate with p(g3T2-T) undoped, 5 mg/mL and 10 mg/mL dopants, following procedures explained in Section 3.5.3.1.

### 4.2.1 Influence of Doping on OEET Channel

Our ultimate goal is to study fully patterned solid-state OEETs that will enable integrated circuits (IC) and thermodynamics studies [43]. To achieve this, it was imperative to initially investigate the isolated impact of channel doping on our devices. Several hypothesis were formulated, based on reference [3]:

1. Modifying channel doping may negatively impact transfer characteristics.
2. The introduction of ionic species ( $\text{TCNQ}^-$ ) into p(g3T2-T) should result in depletion-mode devices with positive threshold voltages. This is because a higher positive gate bias would be needed to counteract these anions and turn off the device.

As explained in the previous chapter, we paired our channel with a non-polarizable gate such as a Ag/AgCl, a widely used configuration for investigating OEET-based materials, and coupled it with a Solid-State Electrolyte (SSE) precursor, whose specific composition was outlined in Table 3.3 of Chapter 3. Unfortunately, the sample that used a solution with a dopant concentration of 20 mg/mL exhibited issues with doping homogeneity. While photolithography was still feasible, it could not provide a fair basis for comparison with the other devices. Consequently, this sample will be excluded from our analysis.

The results shown in Figure 4.6, Figure 4.7 and Figure 4.8 correspond to the same device and the same loop on each sample (undoped, 5 mg/mL, and 10 mg/mL dopants) from the same batch of materials. After reporting the analysis of individual devices, a more comprehensive statistical study will be conducted on operational devices from each sample.

It is essential to note that for the statistical analysis of this section, despite our efforts to increase the yields, only 3 or 4 out of the 14 devices were operational on each sample. Further improvements in the photolithography process were necessary and accomplished, and will be detailed in subsequent sections of this chapter.

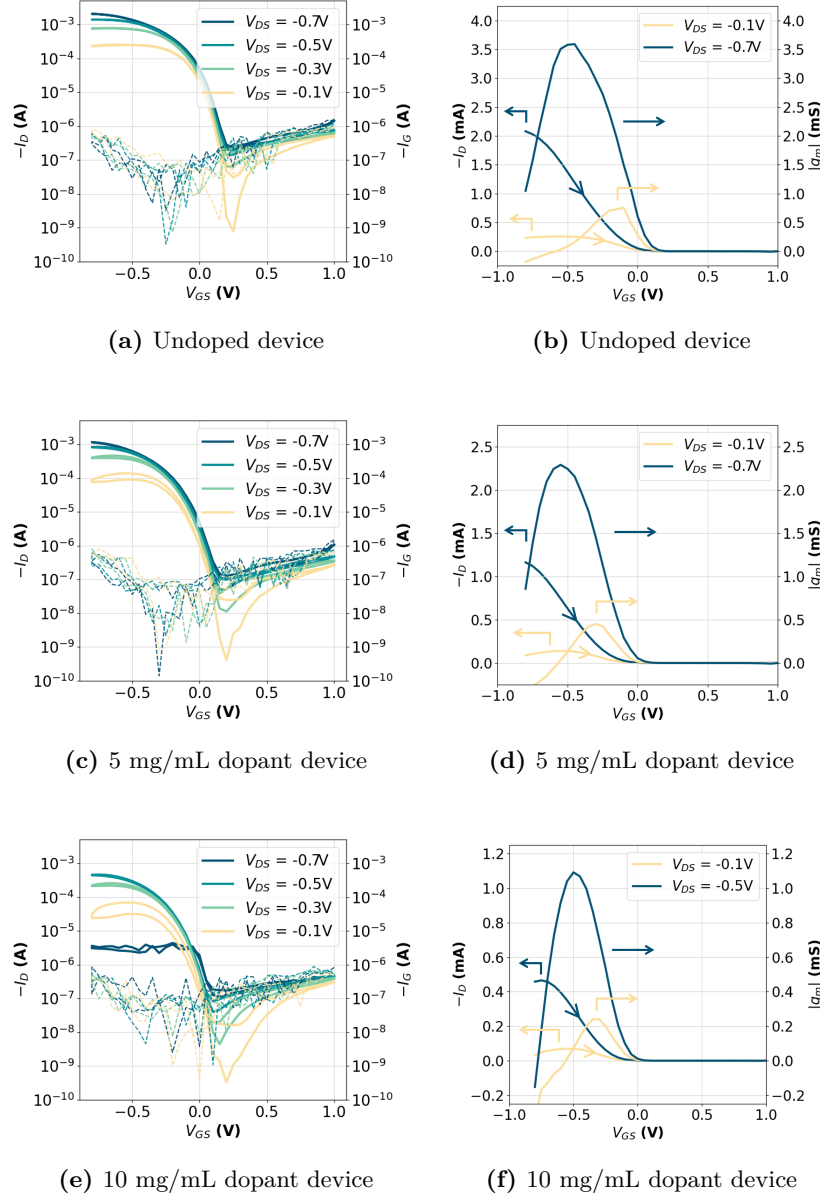
Transfer characteristics are illustrated in Figure 4.6A, C, E, corresponding to undoped, 5 mg/mL, and 10 mg/mL dopants, respectively. Notably, a positive turn-on voltage is observed in the undoped OEET device, indicating the rapid oxidation (unwanted doping) of p(g3T2-T) under environmental conditions due to its low ionization potential (IP).

The drain current ( $I_D$ ) of the undoped device exhibits higher values than doped devices, Hidalgo et al. [44] reported that pristine p(g3T2-T) exhibits oxygen reduction reaction activity in oxygen-saturated conditions, resulting in an increase in current within the polymer until saturation. To address this issue, it will be necessary to control the oxidation state of the polymer during selective steps of the fabrication process or find a way to reverse the oxidation of p(g3T2-T), which will be explored in subsequent sections.

Gate current ( $I_G$ ) is represented by dotted lines, and it is apparent that the drain OFF current ( $I_{D,OFF}$ ) is dominated by this leakage current in all devices.

#### 4. RESULTS AND DISCUSSION

Notably, the device with the highest dopant concentration (10 mg/mL dopant) shows signs of breakage as  $V_{DS}$  becomes more negative (Figure 4.6E and Figure 4.7D). Consequently, this measurement will be excluded from the calculation of transconductance and threshold voltage.

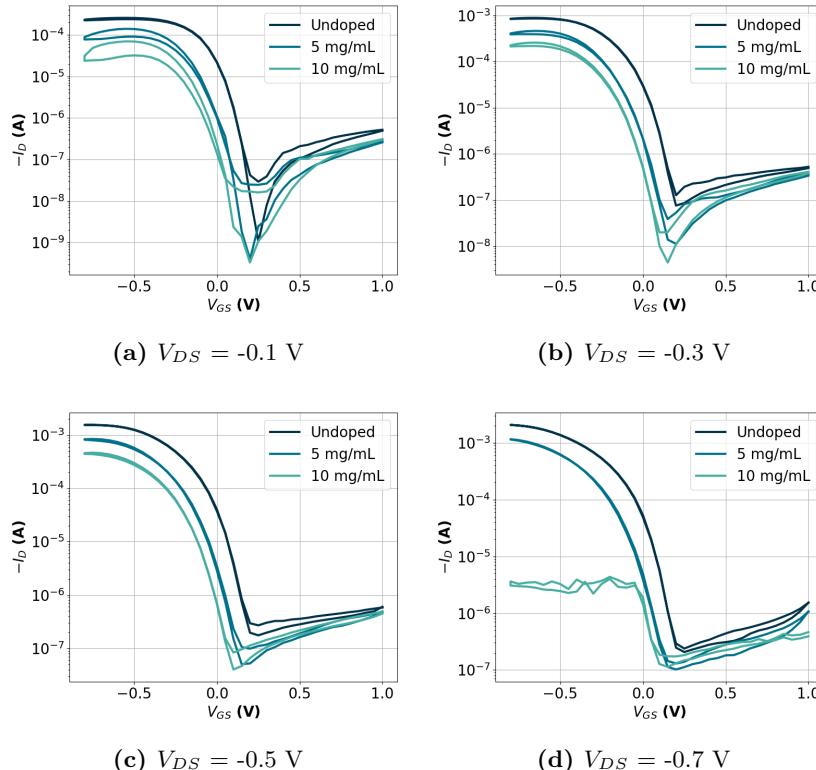


**Figure 4.6:** a), c), e) Transfer characteristics of all measured  $V_{DS}$  including the gate leakage current  $I_G$  b), d), f) Transfer curves (off-switching) with corresponding transconductance. Each group of graphs for undoped, 5 mg/mL and 10 mg/mL doped p(g3T2-T) channel, respectively.

**Table 4.3:** Maximum transconductance values extracted from Figure 4.6

$ g_{m,max} $ [mS] @	Undoped	5 mg/mL	10 mg/mL
$V_{DS} = -0.1$ V	0.75	0.45	0.24
$V_{DS} = -0.3$ V	2.01	1.31	0.74
$V_{DS} = -0.5$ V	2.90	1.97	1.09
$V_{DS} = -0.7$ V	3.59	2.23	

Figure 4.7 illustrates that doped devices exhibit minimal differences in  $I_{D,OFF}$  but there is a noticeable decrease in  $I_{D,ON}$  as the doping levels increase. This is reflected in the maximum transconductance values displayed in Table 4.3, where a clear drop of  $|g_{m,max}|$  is evident with increasing doping levels. This outcome aligns with our initial hypothesis and warrants further investigation with impedance measurements to calculate volumetric capacitance.


**Figure 4.7:** Transfer characteristics comparing undoped, 5 mg/mL and 10 mg/mL dopants devices, each graph represent a different  $V_{DS}$ 

However, a more striking observation is evident in Figure 4.7 and Figure 4.8: the turn-on voltages and threshold voltages, respectively, have shifted towards negative values as the dopant concentration increased in all  $V_{DS}$  values, contradicting our initial hypothesis. This suggest a kind of “compensation doping effect”

## 4. RESULTS AND DISCUSSION

---

in the OECTs, which requires further investigation and resolution.

Additionally, threshold voltage values exhibited lower variability among different  $V_{DS}$  values with higher doping levels, are depicted in Figure 4.8. In the undoped device, the variability could be attributed to oxygen reduction reaction (ORR), which may differ under different drain bias conditions. In contrast, in the doped devices, this variability is expected to decrease since doping depletes reactive electrons from p(g3T2-T) with  $F_6TCNNQ$ , ensuring better stability in air [3].

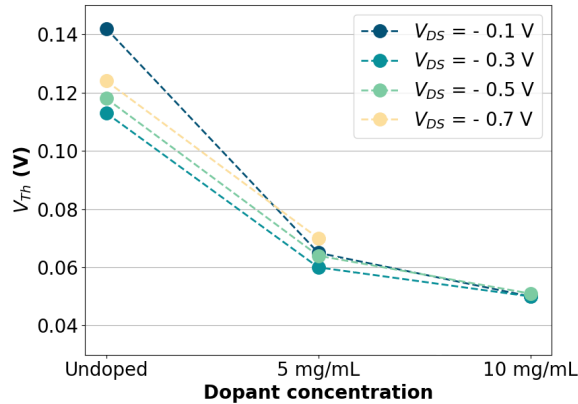


**Figure 4.8:** Threshold shift at different doping levels and  $V_{DS}$ , calculations were done using data shown in Figure 4.6.

Furthermore, while not presented in this report, it was observed during the analysis, that undoped OECT devices exhibit higher repeatability in transfer characteristics (or Appendix?). The saturation of ORR in undoped species, as mentioned earlier, may contribute to this repeatability. However, the variability in doped species requires further study.

### 4.2.2 Stability on Air of p(g3T2-T)

The channel conductivity of an undoped device was measured immediately after spin-coating, yielding a value of  $1 \mu\text{S}$ . After undergoing the patterning process described in the previous sections, the conductivity increased three orders of magnitude to approximately  $1 \text{ mS}$ . Even though,  $\mu\text{S}$  values already signify oxidation, the patterning process further oxidizes our material.

Measurements of  $I_D$  at  $-0.3 \text{ V}$  of  $V_{DS}$  and no gate bias exhibited a small decrease of 4% and small increase of 15% within two hours in  $N_2$  and ambient air environments, respectively. This observation suggests that stability in ambient air is compromised due to unwanted doping.

A similar study was conducted with a doped device containing  $5 \text{ mg/mL}$  of  $F_6TCNNQ$  dopant, resulting a higher level of doping compared to  $F_4TCNQ$  at the same concentration, as detailed in Appendix A. The channel conductivity reached a value of  $266 \mu\text{S}$  with a reduction of 1.2% within one hour in  $N_2$  environment and remained stable with minimal fluctuations of 1.0% within one hour in ambient

## 4.2. Fabrication of Organic Electrochemical Transistors

condition. This indicates a lower conductivity compared to the oxidized p(g3T2-T) but similar stability in air, as reported in reference [3].

Remarkably, upon contact with SSE precursor, conductivity of both samples drops significantly, approximately six orders of magnitude, in an  $N_2$  environment, reaching the sensitivity limits of our equipment and resulting in a noisy signal, as shown in Figure 4.9A. One plausible explanation is that p(g3T2-T), as a type VI OMIEC, lacks chemical binding with  $TCNQ^-$  anions. When in contact with the electrolyte, the anions are drawn away from the polymer backbone (de-doping), restoring its original insulating state. However, it may be possible that cations from the electrolyte could enter the polymer film and neutralize the anions. Further experiments would be needed to clarify both positions. Either way, having a low conductivity polymer film is essential for accumulation-mode OECTs.

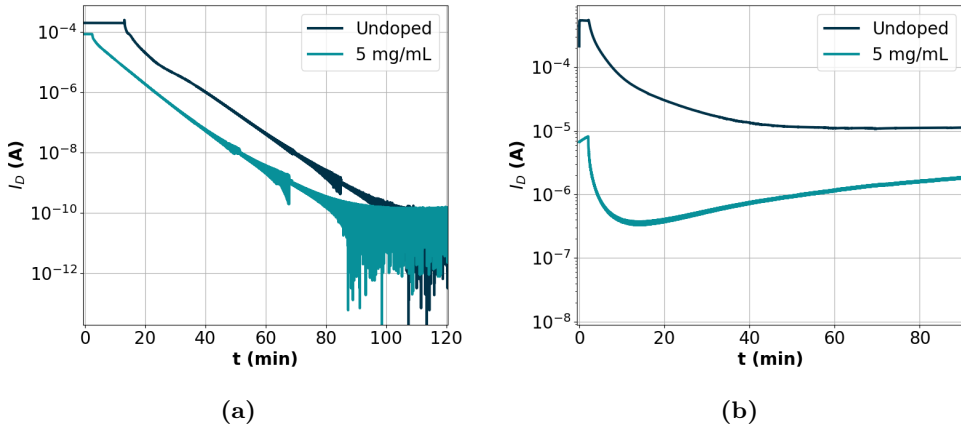


**Figure 4.9:** Drain current over time of undoped p(g3T2-T) coupled with SSE precursor under a)  $N_2$ , and b) ambient environment.

Under ambient conditions, there is a smaller decrease of slightly more than one order of magnitude for the undoped sample, as seen in Figure 4.9B. The doped sample initially exhibited a similar but faster drop within the first 15 minutes, followed by a sudden increase of  $I_D$ . In both scenarios, the ORR prevented a greater decrease in current. The fluctuation seen in the doped species may be attributed to the simultaneous occurrence of irreversible de-doping  $TCNQ^-$  anions and ORR .

Transfer curves of the undoped device using an Ag/AgCl pellet as gate, were measured under ambient conditions after de-doping in  $N_2$  environment, as depicted in Figure 4.10. The device exhibited shifts in its ON voltage and negative threshold voltages values, as summarized in Table 4.4, moving towards negative values. A visible sign of degradation was perceived at the end of the measurements when  $V_{DS}$  is -0.1 V.

In summary, a pre de-doping step could potentially serve as a method for obtaining accumulation-mode OECTs by reversing the oxidation of p(g3T2-T), and will be explored in the following section.

## 4. RESULTS AND DISCUSSION

---

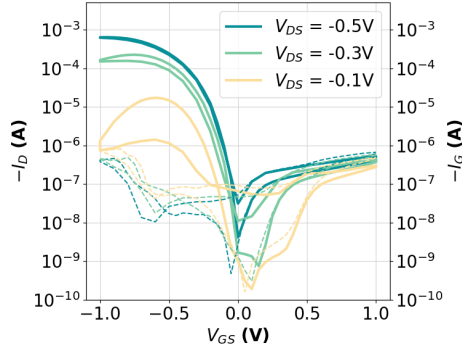


**Figure 4.10:** Transfer characteristics after electrochemical de-doping at different  $V_{DS}$  under ambient conditions

**Table 4.4:** Threshold voltage extracted from Figure 4.10

$V_{DS}$ [V]	$V_{Th}$ [V]
-0.1	-0.18
-0.3	-0.15
-0.5	-0.13

### 4.2.3 Reverse Oxidation of Undoped-p(g3T2-T)

Based on the previous analysis, it took approximately two hours to fully de-dope p(g3T2-T) and reach an insulating state of the polymer. However, this process could be expedited by applying a positive gate bias to one of the devices.

Additionally, the use of high-temperature baking step to revert the oxidation of an p(g3T2-T) OECT will also be tested.

#### 4.2.3.1 By Electrochemical Dedoping

De-doping in a  $N_2$  environment was performed by applying a +1 V gate bias. p(g3T2-T) reached its insulating state in less than 300 seconds, significantly faster than observed in the previous section. However, it was expected that this process would not be reversible upon disconnection of the gate. Figure 4.11A confirms this expectation: after  $I_D$  drastically dropped and the gate was disconnected (gray arrows), the current remained low, and leakage current is predominant. When the gate was reconnected (gold arrows), a capacitive current spike occurred but later stabilized to match the leakage current.

Transfer curves using the p(g3T2-T) gate showed a negative turn-on voltage after reversing oxidation (Figure 4.11B). Additionally, a transfer curve was measured after exposure to UV light. The monomer units in the SSE (NIPAm and HHPA) cross-link upon exposure forming the polymer poly(N-isopropylacrylamide) (PNIPAm), then an increase in current upon crosslinking is observed.

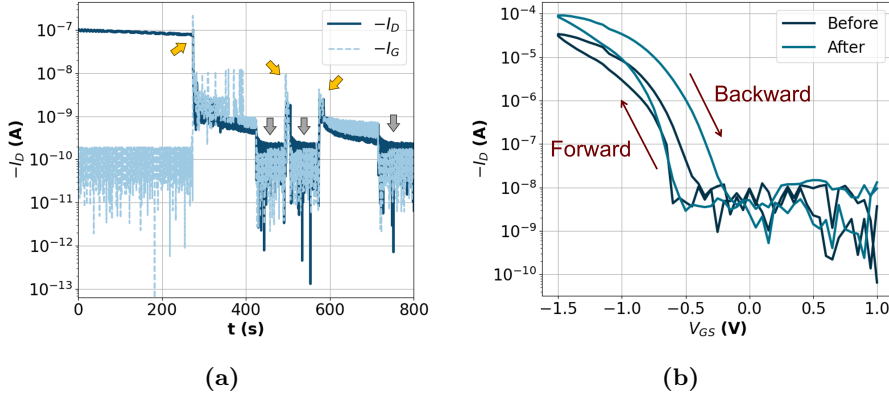


**Figure 4.11:** a) De-doping p(g3T2-T) using a gate biased of +1V, gold arrows indicate gate connection, while grey arrows indicate when gate was disconnected. b) Transfer characteristic before and after exposure at  $V_{DS}$  of -0.1 V using p(g3T2-T) gate coupled with SSE precursor.

Moreover, it was perceived that using the OMIEC gate instead of the Ag/AgCl pellet affects our “gating efficiency”, as expected. Weissbach et al. [45] demonstrated the Electrochemical Electrode Coupling (ECC) between channel and its electrode has a more pronounced effect on device operation when micro-integrated polarizable gates (OMIECs) are used. This can result in saturation loss (as seen in Figure 4.11B) and threshold voltage roll-off when increasing  $V_{DS}$ . This was observed during measurements. Therefore, moving forward,  $V_{DS}$  will be fixed at -0.1 V.

#### 4.2.3.2 By Heating

#### 4.2.4 Solid-OECTs using Undoped-p(g3T2-T)

The fabrication of OECTs using a solid-state electrolyte at IAPP was established in reference [4], the electrolyte that formed PNIPAm is more precisely considered as a rigid gel.

Two types of OECTs were tested under a  $N_2$  environment and later exposed to ambient conditions. In one type, SSE couples all fourteen devices in the sample, while in the other type, each device possesses a microstructure SSE. The latter strategy enhances the performance of OECTs by minimizing leakage current and avoiding device crosstalk. This can be achieved through a photolithography process, as outlined in reference [4], or by inkjet printing, as implemented by team members. Both methods were employed under normal cleanroom conditions to determine which approach minimizes oxidation or allows for the reverse oxidation of p(g3T2-T) within the process.

In this subsection, a total of three samples will be analyzed, it is expected to have low degree of oxidation in all devices.

## 4. RESULTS AND DISCUSSION

---

### 4.2.4.1 OECT with Drop-casted SSE

At this point, the patterning process had improved its yield, with twelve out of the fourteen devices being successfully patterned, although there were some variations in thickness, as evidenced by the reflection hue of the micrographs. Among these devices, only seven remained operational.

Electrochemical de-doping of one device in the sample was carried out before exposure. Measurements of channel conductivity of the other devices indicated an impact of this process to neighboring devices (a total of 5) as most of them had very low conductivity, in the order of nS. One exception exhibited a conductivity in the order of  $\mu$ S and a threshold voltage of 0.0 V. Moreover, attempts to perform irreversible electrochemical de-doping on this device after exposure (cross-linking of monomer units) were unsuccessful. It appeared that the formation of PNIPAm prevented irreversible de-doping. This outcome is crucial for the fabrication of doped-devices and will be discussed further in Section 4.2.5.

Four devices from the sample were measured under the same conditions as detailed in Chapter 3 Section 3.5.3.4. A representative device can be seen in Figure 4.12A, transfer characteristics exhibited a  $|g_{m,max}|$  value of . Threshold voltages were calculated for forward and backward scans, that led to values of 0.09V and -0.06V, respectively, exhibiting a small hysteresis, but further analysis was considered beyond the scope of this work.

From EIS measurements, and by fitting into the equivalent circuit model (inset image at Figure 4.12c) lead to  $C_{channel}$  to 34.0 nF and C\* calculations yield to  $36.5 \text{ F cm}^{-3}$ . Cyclic voltammetry measurements gave oxidation and reduction peaks of +0.65 V and -0.08 V, respectively with a smaller but significant reduction peaks at -0.32 V and -0.01 V.

It is important to clarify that the redox peaks extracted from these measurements do not exclusively represent reduction and oxidation potentials between the working electrode (Au/p(g3T2-T)) and electrolyte. This is because the counter electrode and reference electrode are shorted and connected to the channel, which should be significantly large to minimize its effects on the electrolyte. Instead, these peaks represent crucial operation points for our OECT, where electron transfer is more pronounced.

For instance, the oxidation peak may signify both the oxidation and the reduction of the channel, and the same applies to the reduction peaks. Furthermore, particularly for this case, peaks occurring away from the vicinity of 0 V could indicate interaction with oxygen or the presence of defects in our devices.

A more statistical analysis on the four devices are shown in Table 4.5. Importantly, negative threshold voltages were calculated in all devices with low conductivity. Very low values of capacitance were obtained, which may indicate ongoing oxidation? or the presence of defects (i.e. remnants of photoresist).

Upon exposure to ambient conditions, a negative threshold voltage was maintained (-0.14 V with Ag/AgCl pellet), suggesting that drop-casted SSE creates a protective barrier against molecular oxygen.

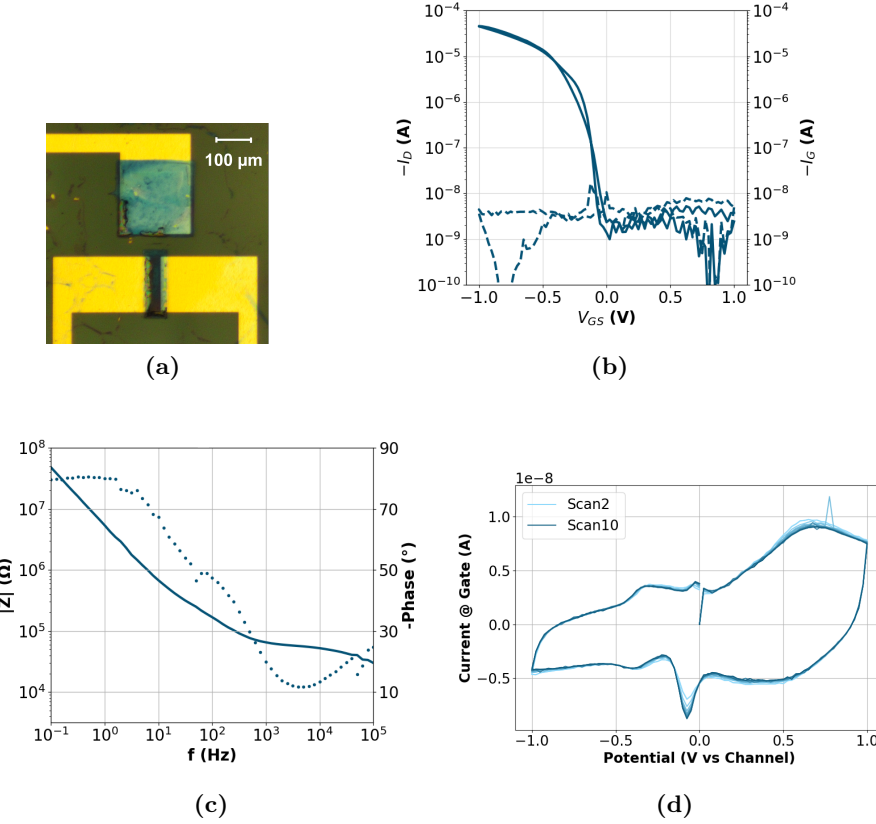


**Figure 4.12:** a) Micrograph of patterned device before application of SSE, b) transfer characteristics at  $V_{DS}$  of -0.1 V. And representative c) Bode plot obtained by EIS and d) redox behavior between Au/p(g3T2-T) and SSE using CV.

**Table 4.5:** Parameters extracted from the characterization of drop-casted SSE OECT

Parameters	Value	Parameters	Value
$V_{Th,forward}$ [V]	$-0.21 \pm 0.13$	$V_{Th,backward}$ [V]	$-0.17 \pm 0.08$
$C_{channel}$ [nF]	$40.9 \pm 12.2$	$C^*$ [ $\text{Fcm}^{-3}$ ]	$43.9 \pm 13.1$
$V_{ox}$ [V]	$0.68 \pm 0.02$	$V_{red}$ [V]	-1.0, -0.1
$ g_{m,max} $ [ $\mu\text{S}$ ]			

#### 4.2.4.2 OECT with Photopatterned SSE

This trial resulted in ten out of fourteen operational devices. A micrograph of a representative device can be seen in Figure 4.13A. However, some devices exhibited unusual behavior due to defects and SSE partially blew off the device, and were excluded from the analysis.

The microstructure SSE on top of the device required the use of an adhesion

#### 4. RESULTS AND DISCUSSION

---

promoter, unlike drop-casted SSE. In this particular case, where the removal of non-crosslinked SSE precursor was achieved using a  $N_2$  gun, the risk of blowing off crosslinked SSE was not as high with the use of an adhesion promoter. Furthermore, the ethanol rinsing and high-temperature baking helped to counteract the oxidation of the polymer. The former led to the reaction described below:



The micrograph in Figure 4.13A represents a patterned device before the application of the adhesion promoter, and signs of oxidation are evident by the brownish hue.

After the application of SSE precursor and exposure, the transfer curves (seen in Figure 4.13B) indicate slight hysteresis, turn-on voltages close to zero, and slightly negative threshold voltages, as shown in Table 4.6. These values are higher compared to the samples with drop-casted SSE.

Cyclic voltammetry measurements gave oxidation and reduction peaks of -0.3 V and -0.1 V, with some smaller oxidation peaks at 0.6 V and -0.2 V.

The channel and volumetric capacitance shows a clear increase compared to drop-casted SSE. However, CV graphs exhibit two different behaviors, with oxidation and reduction potentials falling into the ranges represented in Table 4.6, suggesting that some oxidation is still perceived in most devices.

**Table 4.6:** Parameters extracted from the characterization of photopatterned SSE OECT under  $N_2$  environment.

Parameters	Value	Parameters	Value
$V_{Th,forward}$ [V]	$-0.08 \pm 0.05$	$V_{Th,backward}$ [V]	$-0.09 \pm 0.04$
$C_{channel}$ [nF]		$C^*$ [ $Fcm^{-3}$ ]	
$V_{ox}$ [V]	0.04, 0.34	$V_{red}$ [V]	-0.1, -0.2
$ g_{m,max} $ [ $\mu S$ ]	149		

Upon exposure to ambient environment, measurements revealed depletion-mode devices with a positive gate bias. Suggesting that, unlike drop-casted SSE, photopatterned SSE does not provide sufficient “shielding” to prevent oxidation of p(g3T2-T).

Figures

Table with parameters.

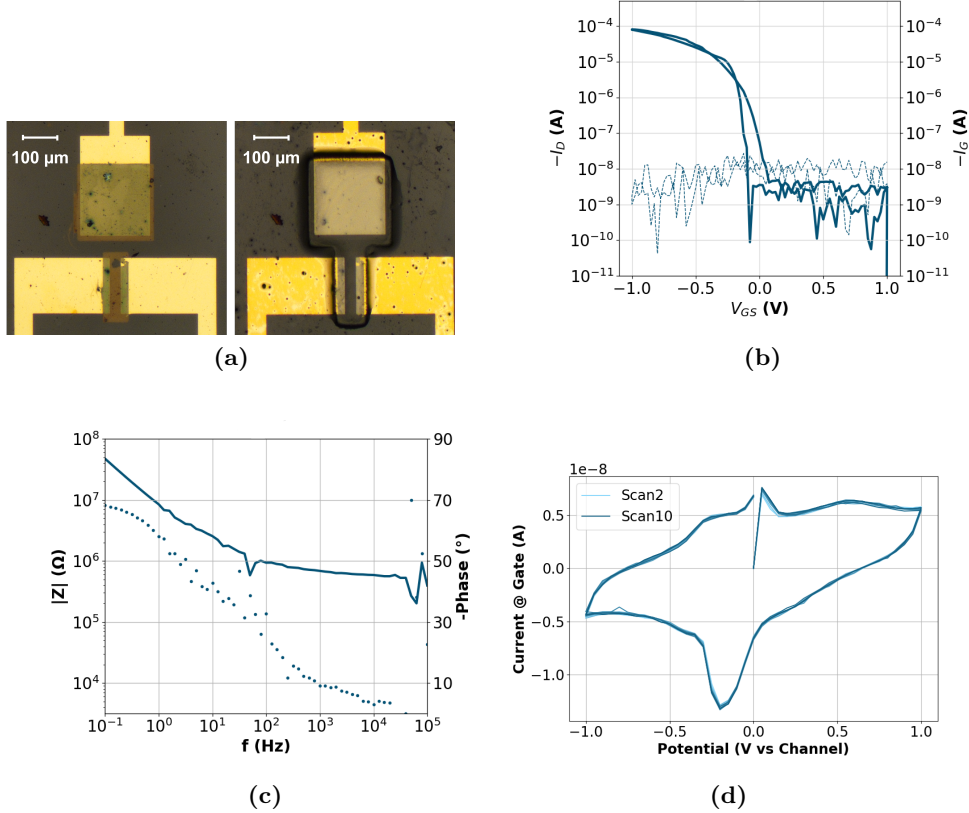


**Figure 4.13:** a) Micrograph of patterned device before and after application of SSE, b) transfer characteristics at  $V_{DS}$  of -0.1 V. And representative c) Bode plot obtained by EIS and d) redox behavior between Au/p(g3T2-T) and SSE using CV.

**Table 4.7:** Parameters extracted from the characterization of photopatterned SSE OECT under ambient conditions

Parameters	Value	Parameters	Value
$V_{Th,forward}$ [V]		$V_{Th,backward}$ [V]	
$C_{channel}$ [nF]		$C^*$ [ $\text{Fcm}^{-3}$ ]	
$V_{ox}$ [V]		$V_{red}$ [V]	
$ g_{m,max} $ [ $\mu\text{S}$ ]	370		

#### 4.2.4.3 OEET with Inkjet-Printed SSE

Despite high yields in the patterning process, only four devices were successfully printed. Out of which, only one was fully operational, and it will be used in this analysis.

The process of printing SSE on top of the patterned gate and channel p(g3T2-T) remains a challenge. The process takes approximately 2 hours per sample under

#### 4. RESULTS AND DISCUSSION

ambient conditions. Efforts were made to set the printing parameters using a different sample while exposing our device to high temperatures and ethanol rinsing to revert oxidation. Unfortunately, the resulted device still exhibited signs of oxidation.

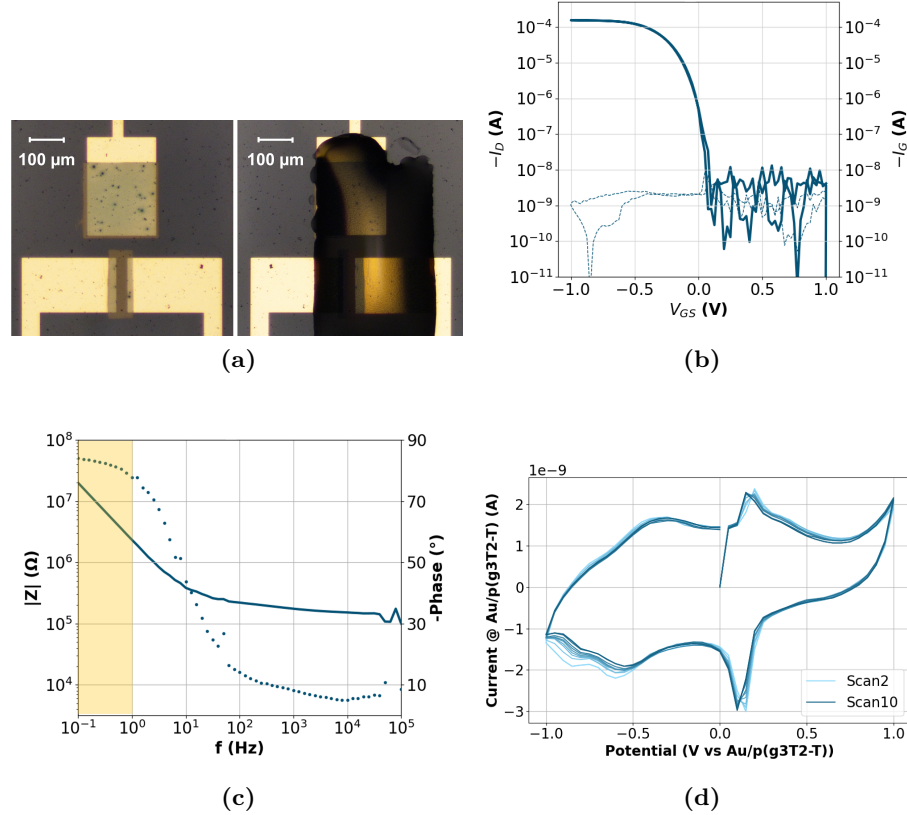


**Figure 4.14:** a) Micrograph of patterned device with printed SSE, b) transfer characteristics at  $V_{DS}$  of -0.1 V. c) Bode plot obtained by EIS and d) redox behavior between Au/p(g3T2-T) and SSE using CV.

**Table 4.8:** Parameters extracted from the characterization of printed SSE OECT

Parameters	Value	Parameters	Value
$V_{Th}$ [V]	0.13	$ g_{m,max} $ [ $\mu\text{S}$ ]	355
$C_{channel}$ U5[nF]	85.3	$C^*$ [ $\text{Fcm}^{-3}$ ]	91.6
$V_{ox}$ [V]		$V_{red}$ [V]	
$C_{channel}$ D6 [nF]	289	$C^*$ [ $\text{Fcm}^{-3}$ ]	311

### 4.2.5 Solid-OECTs using Doped-p(g3T2-T)

#### 4.2.5.1 Channel conductivity

The channel conductivity was monitored using SSE precursor after exposure, and the  $I_D$  no longer decreased but maintained its initial values of ... mS, as seen in Figure ...

Different doping levels were intended to be studied in this section. However, only 5 mg/mL of F<sub>6</sub>TCNNQ showed doping homogeneity that would allow a fair comparison. Figure ... shows irregularities in the doping when using 10 and 15 mg/mL of dopant concentration. Acetonitrile solvent was unable to correctly dissolve this dopant, and achieving higher dopant concentration that may led to depletion-mode OECTs was not possible.

#### 4.2.5.2 Solid-OECT performance

The adhesion promoter used for undoped p(g3T2-T) could not be used for doped species since it will remove dopants during the application steps. An alkaline adhesion promoter would be needed, which required additional experiments to test its effectiveness. Therefore, no promoter was used at these stage, so low yields in printing were expected despite the high yields in patterning.

Eight operational devices were obtained. However, only one exhibited a capacitive behavior that allowed for transfer characteristics, and it will be used in this analysis. Transfer characteristics, EIS and CV measurements are shown in Figure 4.15, and the calculated parameters are exhibited in Table 4.9.

**Table 4.9:** Parameters extracted from the characterization of doped-p(g3T2-T) OECT

Parameters	Value	Parameters	Value
V <sub>Th</sub> [V]	-0.1	g <sub>m,max</sub>   [ $\mu$ S]	567
C <sub>channel</sub> [nF]	130	C* [Fcm <sup>-3</sup> ]	140
V <sub>ox</sub> [V]	0.1	V <sub>red</sub> [V]	0.0

#### 4. RESULTS AND DISCUSSION

---

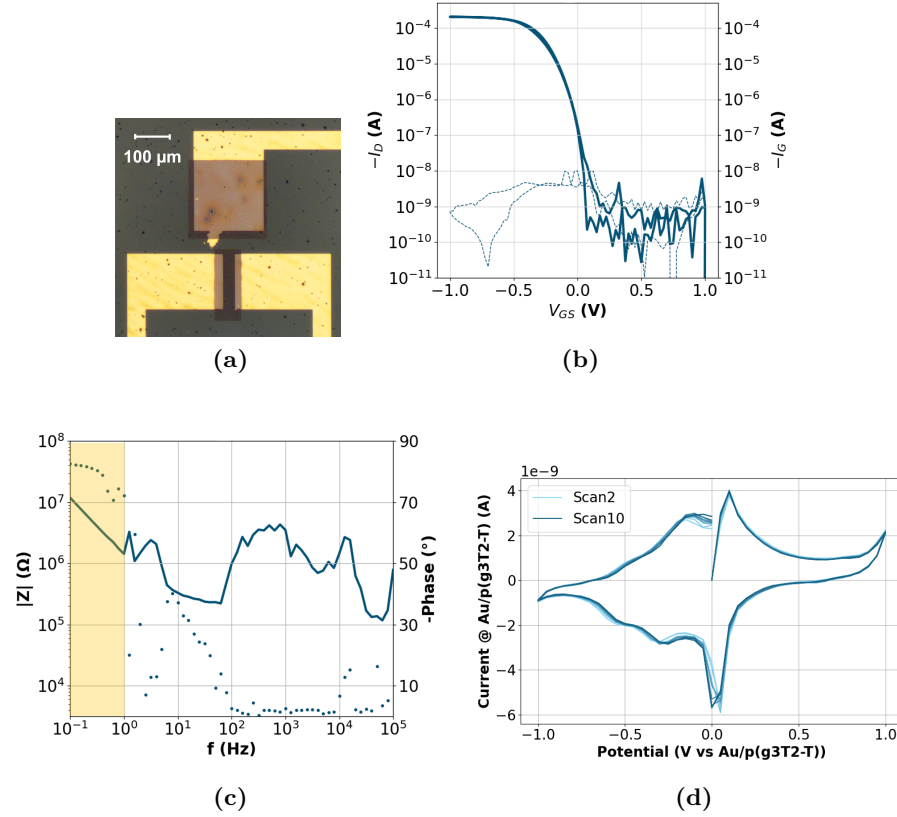


**Figure 4.15:** a) Micrograph of patterned device with printed SSE, b) transfer characteristics at  $V_{DS}$  of -0.1 V. c) Bode plot obtained by EIS and d) redox behavior between Au/p(g3T2-T) and SSE using CV.

##### 4.2.6 Shift of OECT Threshold Voltage

## **Chapter 5**

# **Conclusions and Outlook**



## **Appendix A**

### **Absorption of p(g3T2-T) Doped with F6TCNNQ**



## Appendix B

### PEDOT:PSS vs Doped p(g3T2-T) as Channel



# Bibliography

- [1] J. Rivnay, S. Inal, A. Salleo, R. M. Owens, M. Berggren, and G. G. Malliaras, “Organic electrochemical transistors,” *Nature Reviews Materials*, vol. 3, no. 2, pp. 1–14, 2018.
- [2] C. B. Nielsen, A. Giovannitti, D.-T. Sbircea, E. Bandiello, M. R. Niazi, D. A. Hanifi, M. Sessolo, A. Amassian, G. G. Malliaras, J. Rivnay, and I. McCulloch, “Molecular Design of Semiconducting Polymers for High-Performance Organic Electrochemical Transistors,” *Journal of the American Chemical Society*, vol. 138, no. 32, pp. 10 252–10 259, 2016.
- [3] S. T. M. Tan, G. Lee, I. Denti, G. LeCroy, K. Rozylowicz, A. Marks, S. Griggs, I. McCulloch, A. Giovannitti, and A. Salleo, “Tuning Organic Electrochemical Transistor Threshold Voltage using Chemically Doped Polymer Gates,” *Advanced Materials*, vol. 34, no. 33, p. 2202359, 2022.
- [4] A. Weissbach, L. M. Bongartz, M. Cucchi, H. Tseng, K. Leo, and H. Kleemann, “Photopatternable solid electrolyte for integrable organic electrochemical transistors: Operation and hysteresis,” *Journal of Materials Chemistry C*, vol. 10, no. 7, pp. 2656–2662, 2022.
- [5] L. Alcácer, *Electronic Structure of Organic Semiconductors: Polymers and Small Molecules*. Morgan & Claypool Publishers, Dec. 2018.
- [6] A. J. Heeger, S. Kivelson, J. R. Schrieffer, and W. P. Su, “Solitons in conducting polymers,” *Reviews of Modern Physics*, vol. 60, no. 3, pp. 781–850, Jul. 1988.
- [7] M. Heydari Gharahcheshmeh and K. K. Gleason, “Texture and nanostructural engineering of conjugated conducting and semiconducting polymers,” *Materials Today Advances*, vol. 8, p. 100086, Dec. 2020.
- [8] J. L. Bredas, B. Themans, J. M. Andre, R. R. Chance, and R. Silbey, “The role of mobile organic radicals and ions (solitons, polarons and bipolarons) in the transport properties of doped conjugated polymers,” *Synthetic Metals*, vol. 9, no. 2, pp. 265–274, Apr. 1984.
- [9] B. Lüssem, M. Riede, and K. Leo, “Doping of organic semiconductors,” *physica status solidi (a)*, vol. 210, no. 1, pp. 9–43, 2013.

## BIBLIOGRAPHY

---

- [10] M. L. Tietze, L. Burtone, M. Riede, B. Lüssem, and K. Leo, “Fermi level shift and doping efficiency in \$p\$-doped small molecule organic semiconductors: A photoelectron spectroscopy and theoretical study,” *Physical Review B*, vol. 86, no. 3, p. 035320, Jul. 2012.
- [11] J. L. Bredas and G. B. Street, “Polarons, bipolarons, and solitons in conducting polymers,” *Accounts of Chemical Research*, vol. 18, no. 10, pp. 309–315, Oct. 1985.
- [12] D. Kiefer, R. Kroon, A. I. Hofmann, H. Sun, X. Liu, A. Giovannitti, D. Stegerer, A. Cano, J. Hyynnen, L. Yu, Y. Zhang, D. Nai, T. F. Harrelson, M. Sommer, A. J. Moulé, M. Kemerink, S. R. Marder, I. McCulloch, M. Fahlman, S. Fabiano, and C. Müller, “Double doping of conjugated polymers with monomer molecular dopants,” *Nature Materials*, vol. 18, no. 2, pp. 149–155, Feb. 2019.
- [13] M. T. Fontana, D. A. Stanfield, D. T. Scholes, K. J. Winchell, S. H. Tolbert, and B. J. Schwartz, “Evaporation vs Solution Sequential Doping of Conjugated Polymers: F<sub>4</sub>TCNQ Doping of Micrometer-Thick P3HT Films for Thermoelectrics,” *The Journal of Physical Chemistry C*, vol. 123, no. 37, pp. 22 711–22 724, Sep. 2019.
- [14] I. E. Jacobs, E. W. Aasen, J. L. Oliveira, T. N. Fonseca, J. D. Roehling, J. Li, G. Zhang, M. P. Augustine, M. Mascal, and A. J. Moulé, “Comparison of solution-mixed and sequentially processed P3HT:F4TCNQ films: Effect of doping-induced aggregation on film morphology,” *Journal of Materials Chemistry C*, vol. 4, no. 16, pp. 3454–3466, Apr. 2016.
- [15] S. T. M. Tan, “Organic Mixed Ionic Electronic Conductors for Electrochemical Devices,” Ph.D. dissertation, Stanford University, Palo Alto, CA, Dec. 2022.
- [16] A. Giovannitti, R. B. Rashid, Q. Thiburce, B. D. Paulsen, C. Cendra, K. Thorley, D. Moia, J. T. Mefford, D. Hanifi, D. Weiyuan, M. Moser, A. Salleo, J. Nelson, I. McCulloch, and J. Rivnay, “Energetic Control of Redox-Active Polymers toward Safe Organic Bioelectronic Materials,” *Advanced Materials*, vol. 32, no. 16, p. 1908047, 2020.
- [17] G. A. Snook, P. Kao, and A. S. Best, “Conducting-polymer-based supercapacitor devices and electrodes,” *Journal of Power Sources*, vol. 196, no. 1, pp. 1–12, Jan. 2011.
- [18] Y. Liang, Z. Tao, and J. Chen, “Organic Electrode Materials for Rechargeable Lithium Batteries,” *Advanced Energy Materials*, vol. 2, no. 7, pp. 742–769, 2012.
- [19] B. D. Paulsen, K. Tybrandt, E. Stavrinidou, and J. Rivnay, “Organic mixed ionic–electronic conductors,” *Nature Materials*, vol. 19, no. 1, pp. 13–26, Jan. 2020.

- [20] S. Wang, M. Ha, M. Manno, C. Daniel Frisbie, and C. Leighton, “Hopping transport and the Hall effect near the insulator–metal transition in electrochemically gated poly(3-hexylthiophene) transistors,” *Nature Communications*, vol. 3, no. 1, p. 1210, Nov. 2012.
- [21] S. T. M. Tan, A. Gumyusenge, T. J. Quill, G. S. LeCroy, G. E. Bonacchini, I. Denti, and A. Salleo, “Mixed Ionic–Electronic Conduction, a Multifunctional Property in Organic Conductors,” *Advanced Materials*, vol. 34, no. 21, p. 2110406, 2022.
- [22] J. T. Friedlein, R. R. McLeod, and J. Rivnay, “Device physics of organic electrochemical transistors,” *Organic Electronics*, vol. 63, pp. 398–414, Dec. 2018.
- [23] D. A. Bernards and G. G. Malliaras, “Steady-State and Transient Behavior of Organic Electrochemical Transistors,” *Advanced Functional Materials*, vol. 17, no. 17, pp. 3538–3544, 2007.
- [24] S. Inal, G. G. Malliaras, and J. Rivnay, “Benchmarking organic mixed conductors for transistors,” *Nature Communications*, vol. 8, no. 1, p. 1767, Nov. 2017.
- [25] S. T. Keene, T. P. A. van der Pol, D. Zakhidov, C. H. L. Weijtens, R. A. J. Janssen, A. Salleo, and Y. van de Burgt, “Enhancement-Mode PEDOT:PSS Organic Electrochemical Transistors Using Molecular De-Doping,” *Advanced Materials*, vol. 32, no. 19, p. 2000270, 2020.
- [26] M. Moser, L. R. Savagian, A. Savva, M. Matta, J. F. Ponder, T. C. Hidalgo, D. Ohayon, R. Hallani, M. Reisjalali, A. Troisi, A. Wadsworth, J. R. Reynolds, S. Inal, and I. McCulloch, “Ethylene Glycol-Based Side Chain Length Engineering in Polythiophenes and its Impact on Organic Electrochemical Transistor Performance,” *Chemistry of Materials*, vol. 32, no. 15, pp. 6618–6628, 2020.
- [27] D. Moia, A. Giovannitti, A. A. Szumska, I. P. Maria, E. Rezasoltani, M. Sachs, M. Schnurr, P. R. F. Barnes, I. McCulloch, and J. Nelson, “Design and evaluation of conjugated polymers with polar side chains as electrode materials for electrochemical energy storage in aqueous electrolytes,” *Energy & Environmental Science*, vol. 12, no. 4, pp. 1349–1357, 2019.
- [28] D. Ohayon, V. Druet, and S. Inal, “A guide for the characterization of organic electrochemical transistors and channel materials,” *Chemical Society reviews*, vol. 52, no. 3, pp. 1001–1023, 2023.
- [29] T. Nguyen-Dang, K. Harrison, A. Lill, A. Dixon, E. Lewis, J. Vollbrecht, T. Hachisu, S. Biswas, Y. Visell, and T.-Q. Nguyen, “Biomaterial-Based Solid-Electrolyte Organic Electrochemical Transistors for Electronic and Neuromorphic Applications,” *Advanced Electronic Materials*, vol. 7, no. 12, p. 2100519, 2021.

## BIBLIOGRAPHY

---

- [30] A. Savva, R. Hallani, C. Cendra, J. Surgailis, T. C. Hidalgo, S. Wustoni, R. Sheelamanthula, X. Chen, M. Kirkus, A. Giovannitti, A. Salleo, I. McCulloch, and S. Inal, “Balancing Ionic and Electronic Conduction for High-Performance Organic Electrochemical Transistors,” *Advanced Functional Materials*, vol. 30, no. 11, p. 1907657, 2020.
- [31] A. Savva, C. Cendra, A. Giugni, B. Torre, J. Surgailis, D. Ohayon, A. Giovannitti, I. McCulloch, E. Di Fabrizio, A. Salleo, J. Rivnay, and S. Inal, “Influence of Water on the Performance of Organic Electrochemical Transistors,” *Chemistry of Materials*, vol. 31, no. 3, pp. 927–937, Feb. 2019.
- [32] P. S. Foundation, “Miscellaneous operating system interfaces,” 2001-2023, date last access: 30-May-2023. [Online]. Available: <https://docs.python.org/3/library/os.html>
- [33] ———, “Csv file reading and writing,” 2001-2023, date last access: 30-May-2023. [Online]. Available: <https://docs.python.org/3/library/csv.html>
- [34] N. Developers, “Numpy user guide,” 2008 - 2022, date last access: 30-May-2023. [Online]. Available: <https://numpy.org/doc/stable/user/index.html#user>
- [35] T. S. community, “Scipy.stats.linregress,” 2008-2023, date last access: 30-May-2023. [Online]. Available: <https://docs.scipy.org/doc/scipy/reference/generated/scipy.stats.linregress.html>
- [36] G. avhn, “Peak detect library,” 2022, date last access: 30-May-2023. [Online]. Available: <https://github.com/avhn/peakdetect/blob/master/README.md>
- [37] J. Hunter, D. Dale, E. Firing, M. Droettboom, and M. development team, “Matplotlib: Quick start guide,” 2012 - 2023, date last access: 30-May-2023. [Online]. Available: [https://matplotlib.org/stable/tutorials/introductory/quick\\_start.html](https://matplotlib.org/stable/tutorials/introductory/quick_start.html)
- [38] S. GmbH, “Sheet resistance calculator,” 2023, date last access: 30-May-2023. [Online]. Available: <https://www.suragus.com/en/technology/sheet-resistance-calculator/>
- [39] E. V. I. for Speciation Analysis (EVISA), “Instrument database: Shimadzu europe - solidspec-3700/3700duv,” 2003-2010, date last access: 30-May-2023. [Online]. Available: <https://speciation.net/Database/Instruments/Shimadzu-Europe/SolidSpec37003700DUV-;i1305>
- [40] S. A. Buchholtz, “Doping Properties of Novel Dopants for Organic Hole Transport Layers,” Master’s thesis, Technische Universität Dresden, Dresden, Germany, nov 2021.
- [41] L. M. Bongartz, “Organic electrochemical transistors with solid-state electrolytes,” Master’s thesis, Technische Universität Dresden, Dresden, Germany, Jul. 2021.

## BIBLIOGRAPHY

---

- [42] C. Enengl, S. Enengl, S. Pluczyk, M. Havlicek, M. Lapkowski, H. Neugebauer, and E. Ehrenfreund, “Doping-induced absorption bands in P3HT: Polarons and bipolarons,” *ChemPhysChem*, vol. 17, no. 23, pp. 3836–3844, 2016.
- [43] M. Cucchi, A. Weissbach, L. M. Bongartz, R. Kantelberg, H. Tseng, H. Kleemann, and K. Leo, “Thermodynamics of organic electrochemical transistors,” *Nature Communications*, vol. 13, no. 1, p. 4514, Aug. 2022.
- [44] T. C. Hidalgo Castillo, M. Moser, C. Cendra, P. D. Nayak, A. Salleo, I. McCulloch, and S. Inal, “Simultaneous Performance and Stability Improvement of a p-Type Organic Electrochemical Transistor through Additives,” *Chemistry of Materials*, vol. 34, no. 15, pp. 6723–6733, Aug. 2022.
- [45] A. Weissbach, M. Cucchi, H. Tseng, K. Leo, and H. Kleemann, “Unraveling the Electrochemical Electrode Coupling in Integrated Organic Electrochemical Transistors,” *Advanced Functional Materials*, p. 2302205, Jul. 2023.